

## Spatiotemporally resolved heat dissipation in 3D patterned magnetically responsive hydrogels

### AUTHOR(S)

Patricia Monks, Jacek K Wychowaniec, Eoin McKiernan, Shane Clerkin, John Crean, Brian J Rodriguez, Emmanuel G Reynaud, Andreas Heise, Dermot F Brougham

### CITATION

Monks, Patricia; Wychowaniec, Jacek K; McKiernan, Eoin; Clerkin, Shane; Crean, John; Rodriguez, Brian J; et al. (2021): Spatiotemporally resolved heat dissipation in 3D patterned magnetically responsive hydrogels. Royal College of Surgeons in Ireland. Journal contribution. <https://hdl.handle.net/10779/rcsi.17294384.v1>

### HANDLE

[10779/rcsi.17294384.v1](https://hdl.handle.net/10779/rcsi.17294384.v1)

### LICENCE

CC BY-NC-SA 4.0

This work is made available under the above open licence by RCSI and has been printed from <https://repository.rcsi.com>. For more information please contact [repository@rcsi.com](mailto:repository@rcsi.com)

### URL

[https://repository.rcsi.com/articles/journal\\_contribution/Spatiotemporally\\_resolved\\_heat\\_dissipation\\_in\\_3D\\_patterned\\_magnetically\\_responsive\\_hydrogels/17294384/1](https://repository.rcsi.com/articles/journal_contribution/Spatiotemporally_resolved_heat_dissipation_in_3D_patterned_magnetically_responsive_hydrogels/17294384/1)

**Spatiotemporally resolved heat dissipation in 3D patterned magnetically responsive hydrogels**

*Patricia Monks, Jacek K. Wychowaniec, Eoin M<sup>c</sup>Kiernan, Shane Clerkin, John Crean, Brian J. Rodriguez, Emmanuel G. Reynaud, Andreas Heise, Dermot Brougham\**

B.Sc. P. Monks, Ph.D. J. K. Wychowaniec, B.Sc. E. M<sup>c</sup>Kiernan<sup>1</sup>, Prof. D. Brougham<sup>1\*</sup>

School of Chemistry, University College Dublin, Belfield, Dublin 4, Ireland

E-mail: dermot.brougham@ucd.ie

M.Sc. S. Clerkin, Prof. J. Crean, Prof. B. J. Rodriguez, Prof. E. G. Reynaud

School of Biomolecular and Biomedical Science, University College Dublin, Belfield,

Dublin 4, Ireland

Prof. B. J. Rodriguez

School of Physics, University College Dublin, Belfield, Dublin 4, Ireland

B.Sc. P. Monks, Prof. A. Heise

Department of Chemistry, Royal College of Surgeons in Ireland, Dublin, Ireland

**ORCID numbers of authors:**

**Jacek K. Wychowaniec:** <https://orcid.org/0000-0002-6597-5242>

**Eoin McKiernan:** <https://orcid.org/0000-0003-2685-4592>

**Shane Clerkin:** <https://orcid.org/0000-0002-3493-0439>

**John Crean:** <https://orcid.org/0000-0002-4337-6177>

**Brian J. Rodriguez:** <https://orcid.org/0000-0001-9419-2717>

**Emmanuel G. Reynaud:** <https://orcid.org/0000-0003-1502-661X>

**Andreas Heise:** <https://orcid.org/0000-0001-5916-8500>

**Dermot Brougham:** <https://orcid.org/0000-0002-1270-8415>

Keywords: Spatiotemporal heat release, 3D printing, Magnetic hydrogels, 3D patterning, Hyperthermia

Multifunctional nanocomposites which exhibit well-defined physical properties and encode spatiotemporally controlled responses are emerging as components for advanced responsive systems, *e.g.* in soft robotics or drug delivery. Here an example of such a system, based on simple magnetic hydrogels composed of iron oxide magnetic nanoflowers and Pluronic F127 that generates heat upon alternating magnetic field irradiation is described. Rules for heat-induction in bulk hydrogels and the heat-dependence on particle concentration, gel volume, and gel exposed surface area are established, and the dependence on external environmental conditions in ‘closed’ as compared to ‘open’ (cell culture) system, with controllable heat jumps, of  $\Delta T$  0-12°C, achieved within  $\leq 10$  minutes and maintained described. Furthermore the use of extrusion-based 3D printing for manipulating spatial distribution of heat in well-defined printed features with spatial resolution  $< 150 \mu\text{m}$ , sufficiently fine to be of relevance to tissue engineering, is presented. Finally, localised heat induction in printed magnetic hydrogels is demonstrated through spatiotemporally-controlled release of molecules (in this case the dye methylene blue). The study establishes hitherto unobserved control over combined spatial and temporal induction of heat, the applications of which in developing responsive scaffold remodelling and cargo release for applications in regenerative medicine are discussed.

## 1. Introduction

Native tissues develop and reside within complex and dynamic microenvironments known as the extracellular matrixes (ECM). Spatiotemporal cellular remodelling of ECM influences both the biomechanical and biochemical properties of the microenvironment contributing to regulation of diverse cellular processes including differentiation, migration and tissue homeostasis.<sup>[1-3]</sup> Due to their tuneable physical and biological properties, hydrogels have emerged as appropriate scaffolds for drug delivery and advanced tissue engineering applications.<sup>[4-5]</sup> Hydrogel matrices mimic many aspects of native ECM due to their three-dimensional architecture, extensive water retention capabilities and variable biophysical properties including shape, mechanical strength and permeability.<sup>[6-7]</sup> Hence these static supports are useful for investigating the effect of defined microenvironment properties including the presence of topographical features and variable substrate stiffness and surface chemistry/charge on cell behaviour, however, they do not facilitate stimulus responsive scaffold remodelling or enable tuneable molecular release strategies.

In recent years, the advent of additive manufacturing has enabled fabrication of intricate and customisable scaffolds.<sup>[8-10]</sup> Integrating complex composite hydrogel matrices with three-dimensional (3D) printing technology provides an unprecedented opportunity to more closely recapitulate dynamic *in vivo* structural tissue architecture and generate user-defined instructive cell signalling complexity. Recently, 3D printing was used to fabricate growth-factor bearing heparin-based hydrogels with complex geometries<sup>[10]</sup> which exhibit controllable long-term release rates and switchable delivery sequence through alternating radial layers. However, although spatially patterned, such supports lack temporally controlled responses, which could be triggered by an external stimulus.<sup>[11]</sup>

Nanocomposite materials which combine the tuneable properties of nanoparticles with chemically defined polymer scaffolds represent a powerful means to improve controllability and alter the physicochemical properties of microenvironments *in situ*.<sup>[12]</sup> Suspension of magnetic nanoparticles (MNPs) have been developed for biomedical applications as contrast agents for MRI and for cancer ablation,<sup>[13-17]</sup> with the latter exploiting strong heating on exposure to alternating magnetic fields (AMF) arising due their superparamagnetic properties (rapidly fluctuating moments). MNP polymer nanocomposites can in principle respond to applied AMF to induce structural changes and to programme functional responses such as stimulating time-dependent deformation or release of cargo on demand.<sup>[18-21]</sup> The inclusion of MNPs aligned *in situ* by magnetic fields during gelation has the potential to create composite matrices with well-defined spatial topography to directionally influence growth of cellular protrusions, such as neurites<sup>[22, 23]</sup> or whole cellular constructs, such as organoids.<sup>[24]</sup> 3D printing technologies have already contributed to fabrication of multi-responsive and hierarchically organized soft nanocomposite hydrogels providing well-defined environments for cell manipulation.<sup>[25, 26]</sup>

Many approaches to engineering spatio-temporal control over chemical processes have been reported. Prominent goals include controlling reactions, for instance remote radiofrequency controlled repair of gaps in microwires using magnetically-positionable microfabricated nanolitre-scale delivery systems has been demonstrated.<sup>[27]</sup> More often the goal is stimulus-responsive release of biologically-active species, for instance by near-IR irradiation of thermo-responsive polymer coated gold nanocages,<sup>[28]</sup> or of AMF-responsive degradable polymeric MNP-loaded helical microrobots.<sup>[29]</sup> A range of techniques including; application of asymmetric flow fields; spontaneous and templated self-assembly; laser-writing; layer-by-layer stereolithography, and 2- and 3-D microfluidic network formation have been used to spatially-pattern temporally-

responsive nano- and micro-scale capsules, and these fields have been recently reviewed.<sup>[30]</sup> Finally, AMF enhanced Fenton-like nano-catalytic reactions were recently reported in MNP-loaded printed macroscale composite scaffolds for bone regeneration.<sup>[31]</sup> However, to the best of our knowledge, spatial and temporal control over local AMF response in 3D printed nanocomposite hydrogels to provide stimulated release profiles for regenerative medicine has not been described.

Here we present nano-compositing of AMF-responsive magnetic nanoflowers (MNFs) in thermoresponsive Pluronic F127 hydrogels for the fabrication of novel 3D printable architectures which enable new applications as stimulus-responsive materials. MNFs were selected due to their well-documented excellent AMF-responsive heating, as compared to spherical particles.<sup>[32]</sup> For the purposes of demonstrating the principle of spatio-temporal control we have targeted temperature jumps,  $\Delta T$ , of 5-10 °C over features  $\leq 150$   $\mu\text{m}$  in size and a response time of 1-2 minutes. The target temperature increase would enable localised transitions to above the transition temperature of conventional thermo-responsive polymers such as NIPAAm (LCST *c.* 32 °C) from starting temperatures of 25 °C,<sup>[21]</sup> or above that of high LCST polymers such as NIPMAm (LCST *c.* 42 °C) starting from cell culture conditions, *i.e.* 37 °C.<sup>[33]</sup> The target length scale enables such processes to be controlled across a cell-support network generating temperature gradients for specifying multiplexed cell and organoid stimulus exposure through their location on the support. The target response time provides a platform for pulsed cell culture stimulus, once full morphological and rheological recovery is demonstrated following the pulse ensuring a mechanically stable cell support.<sup>[34]</sup>

The shear-thinning properties of F127 lead to easy fabrication of well-defined spatially resolved structures with rapidly recovery using extrusion-based 3D printing, while retaining sufficient AMF response to provide localised temperature jumps in the target range (depending on concentration).<sup>[35, 36]</sup> For the MNF-pluronic formulations

we demonstrate; (i) reproducible and robust extrusion of magnetic hydrogels; (ii) spatial patterning of thermally active components on the length scale of  $\leq 150\ \mu\text{m}$  with responsive dye release, and; (iii) *in situ* manipulation using AMF stimulation confirmed by high-resolution thermal mapping. The approach we describe could be applied using other platforms for formation of spatially-patterned magnetic hydrogels for many applications.<sup>[25, 26]</sup> These capabilities facilitate control over stimulus response over length scales relevant to tissue engineering and provide potential for high through-put printed gel bed arrays for screening.<sup>[37]</sup> These applications and the technical development of the responsive gels, the 3D printing procedure, and the thermography are described in this article.

## 2. Results and Discussion

### 2.1. Magnetic gel formulation and primary physical characterisation.

Magnetic iron oxide nanoflowers were synthesized using a minor adaptation of the procedure developed by Hugounenq *et al.*<sup>[38]</sup> which produced MNF suspensions with a yield of 49% and a TEM size of  $20.7 \pm 2.5\ \text{nm}$  (with good consistency in shape) and larger average hydrodynamic size of 36.5 nm with low polydispersity index PDI, from the cumulants analysis (see Experimental) of 0.16 (**Figure 1A** and **1B**). It is expected that DLS should give a larger size, in part because it is weighted by the scattering intensity (TEM provides a number average). In this case direct comparisons between the values are further complicated by the fact TEM provides the average particle (tip to tip) size and size variance while DLS gives the average equivalent sphere hydrodynamic size and does not reflect the non-uniformity of the nanoflowers. Taken together the data in demonstrate good MNF dispersion and stability of the resulting aqueous suspensions. Pluronic F127 has previously been described in bio-

inks for 3D printing both as a major component of the final matrix<sup>[35]</sup> and as a fugitive ink;<sup>[39]</sup> it is a relatively soft, easily-handled extrude-able material for spatial patterning using 3D printing technologies. Hence we dissolved biocompatible, thermoresponsive and 3D-printable Pluronic F127 in a solution of MNFs to form magnetic hydrogels (**Figure 1C**).

One of our goals is to evaluate the minimum feature dimensions for which useful hyperthermic responses,  $\Delta T \sim 10^\circ\text{C}$ , can be achieved across a printed hydrogel on applying alternating magnetic field (AMF) stimulus. Hence we first compared the bulk response of 210 mM MNFs in  $\text{H}_2\text{O}$  (MNF-S-210) to 40 w/v% F127-210 mM MNF magnetic hydrogels (MNF-G-210) (**Figure 1D**). Typically hyperthermic responses of homogeneous suspensions were measured in enclosed insulated plastic containers using an optical thermometer, *i.e.* a ‘closed system’, an approach designed to minimise heat dissipation with the surroundings.<sup>[40]</sup> Typical ‘closed system’ hyperthermic responses achieved for the suspension and gels are shown in **Figure 1D** and **Figure 1E**, with temperature jumps after 90 seconds irradiation,  $\Delta T_{90}$ , of  $\sim 47^\circ\text{C}$  and  $\sim 11^\circ\text{C}$  for the at 210 mM Fe concentration, respectively, observed. The responses were repeatable suggesting stability of both samples. The specific absorption rate (SAR) of AC field energy, *i.e.* the hyperthermic efficiency under quasi-adiabatic conditions, is commonly used as a comparison between samples it is defined as;

$$SAR = \frac{C}{m_{Fe}} * \frac{\Delta T}{\Delta t} \quad \text{Equation 1}$$

where C is the heat capacity of a media,  $m_{Fe}$  the mass of iron (in g) and  $\frac{\Delta T}{\Delta t}$  defines an initial slope of the temperature-time plot extracted as the linear term from a 5<sup>th</sup> order polynomial fit, a commonly accepted approach.<sup>[32]</sup> The MNF syntheses yielded aqueous suspensions with  $SAR_{MNF-S}$  of  $309 \pm 26 \text{ W.g}^{-1}$  over this concentration range, an



outcome that is reproducibly observed for nanoflowers in our laboratory. While for the magnetic gels a much reduced apparent (derived using  $C_{H_2O}$ )  $SAR_{MNF-G}$  value of  $43 \pm 6$   $W \cdot g^{-1}$  was measured, over the same concentration range (70, 140 and 210 mM, *i.e.* millimoles Fe per 1 mL of suspension or gel). The error estimation is described in Experimental. The observation of reduced hyperthermic response is commonly observed in magnetic gels and is usually attributed to changes in viscosity or loss of Brownian motion,<sup>[41]</sup> which are known to suppress Brownian contributions to the hyperthermic response, and/or formulation induced particle aggregation, which should primarily suppress the Néel contribution. The observation that the bulk temperature jumps achieved for the magnetic hydrogels are proportional to concentration **Figure 1D**, and the  $SAR_{MNF-G}$  value doesn't change, is consistent with similar particle dispersion in the gels across this loading range. Multiple electron dispersive X-ray spectroscopy (EDX) measurements (see **Figure S1**), which have an associated penetration depth of  $\sim 1 \mu m$  and an intrinsic  $\pm 1\%$  error on elemental composition, from across the MNF-G-70 sample gave values of  $\sim 4$  wt% (Fe) in the dry gel, which is close to the anticipated ratio, from the (dry) formulation of  $\sim 3.2\%$ . This also indicates good dispersion of particles achieved across the surface (at least) of the gel. Detailed analysis of the factors determining the hyperthermic responses of gels is the subject of a forthcoming study. For now we note that sufficient heating, as described in the Introduction, was achieved to further pursue these compositions for our target applications (**Figure 1E**). Furthermore, as the jump observed is highly dependent on both concentration and time, either factor could be used to determine the induced heat response. Controlled thermal dose is critical for balancing the requirements of predictable thermally-responsive delivery<sup>[21, 42]</sup> and for maintaining cell viability.<sup>[43]</sup>

Electrostatic or hydrophobic interactions between the nano-fillers and polymers in hydrogel networks are known to affect the bulk mechanical properties<sup>[44]</sup>

and AMF induced heating itself could irreversibly change the mechanical properties of the hydrogel. It is also known that mechanical strength, in particular the storage modulus ( $G'$ ) can affect cell differentiation and proliferation.<sup>[45]</sup> Hence the temperature-dependent rheological properties of the hydrogels (**Figure 2**) were evaluated. The behaviour of un-loaded and MNF-loaded samples was similar, with  $G'$  values of ~27 kPa measured at 20 °C (**Figure S2E**) and with unchanged amplitude and frequency behaviour irrespective of the Fe concentration (**Figure S2-S3**).  $G'$  was found to increase by ~10 kPa on increasing temperature from 20 to 45 °C, the upper end of our target range, and these changes were found to be fully and rapidly reversible on reducing temperature back down to 20 °C, with symmetrical time-temperature behaviour evident in all cases (**Figure 2**). Hence  $G'$  and  $G''$  are not a function of Fe concentration (at fixed temperature, strain and frequency) in the 0 - 210 mM range.

The observed rapid recovery of stiffness suggests there is little microscopic structural deformation and that gels should be stable to cycled AMF stimulus, as is also suggested by **Figure 2D**. Furthermore the absence of any measurable Fe concentration effect on the moduli suggests mechanical integrity should be maintained across spatially patterned (3D-printed) F127 formulations with separate magnetic and non-magnetic components, even under AMF stimulation, see below. It is well established that rheological properties are very sensitive to polymer-nanofiller interactions<sup>[46]</sup> so the picture that emerges is of the inks as simple mixtures of non-ionic polymer and dispersed MNFs with minimal physical interactions. It can be anticipated that the 3D printability will also not be affected by MNF loading. Hence there may be significant potential for patterned magnetic gels in providing both hyperthermic and mechanical cell stimulus.

In anticipation of 3D printing the ‘magnetic inks’ into well-defined patterns we first evaluated the likelihood of shear forces exerted during extrusion via nozzle by measuring their recoverability to increased applied strain, across the Fe concentration range, (**Figure 3**). The modulus of all the inks was observed to recover completely within a few seconds. Under real 3D printing conditions (see Materials and Methods) excellent feature fidelity was retained (**Figure 3B**); printed structures showed no spread on extrusion; good control over line thickness, and no overlap or smearing of the printed features.

To summarise the findings on the gel stability; the analysis confirms the homogeneity and stability of the gels across the MNF concentration range studied. All gels were stable to AMF-induced and background temperature cycling. Hyperthermic responses were also reproducible upon gel reformation, *i.e.* upon gel-sol-gel re-fabrication by RT-4°C-RT cycling. The samples were stable for months in sealed containers.

## 2.2. Hyperthermic responses of un-patterned magnetic gels.

Hyperthermia applications necessitate more open-environments, especially for cell culture applications, where gas exchange is crucial for cell survival<sup>[47]</sup> and thermal coupling to the surroundings must be good. For evaluating hyperthermic responses of magnetic gels an open AMF irradiation coil that accommodates a standard 35 mm diameter Petri dish was used with a thermal camera to measure spatially resolved *in situ* heat dissipation (*i.e.* in a ‘open system’, see **Figure 4** and **S4**). Note that the temperature calibration is discussed in the thermography section of the Experimental. AMF irradiation of suspensions or gels of a given Fe concentration in the closed as opposed to open system typically yielded higher temperatures jumps due to the conditions being closer to adiabatic (**Figure 4A, B and 1E**), note that the differences in

the frequency and field intensity between the two systems are relatively minor. In the open system, for fixed volume of magnetic hydrogel in our established concentration range, the measured temperature jump over 600 seconds irradiation,  $\Delta T_{600}$ , still lies within our target range; it is a function of particle concentration, and the background heating is minimal. Note also that the average heating for the whole discs (*Figure S5*) is only slightly lower than that of the centre point shown here.

Heat induced in magnetic hydrogels is observed to partially flow towards non-magnetic poured hydrogels (which are heated to slightly above background), as shown for two 0.5 mL poured magnetic and non-magnetic hydrogels in direct contact in *Figure 4C, D*. Some reduction in  $\Delta T$  for this magnetic component, as compared to those at 1 mL volume, is evident demonstrating the expected dependence of induced heating on the volume, and perhaps the surface area, of the magnetic component. *Figure S6* confirms that the average  $\Delta T$  value for whole disc falls exactly between that measured for the magnetic and non-magnetic halves, as expected. To investigate in more depth different volumes of MNF-G-210 were poured into identical Petri dishes (*Figure 4E and 4F*), minimising differences in surface area and maintaining the same upper (air) and lower (glass) surface contacts. A clear relationship between  $\Delta T$  and hydrogel volume is apparent, with significant responses achieved only above 0.1 mL gel volume under the conditions used, the average temporal change across the sample is slightly lower (*Figure S6*) but shows the same trend. Finally, a  $\Delta T_{\max}$  of  $\leq 14$  °C was observed depending on the concentration, when starting at 18-19 °C. In similar experiments starting from 29 °C a  $\Delta T_{\max}$  of  $\leq 8$  °C could be achieved (*Figure S7*). Hence it is clear that, while temperature jumps decrease with increasing background temperature,  $\Delta T$  of 4-6 °C, as per our criteria for cell culture conditions, above, and  $\Delta T$  can be tuned further through the Fe concentration.

To evaluate the effect of the hydrogel surface area the hyperthermic response of MNF-G-210 hand-printed into shapes with differing surface area, but the same, 0.5 or 0.25 mL, volume as the equivalent poured disks (**Figure 4E**), was measured (**Figure S8**). For both volumes higher  $\Delta T_{600}$  was achieved for lower surface areas, as expected, on the basis of heat dissipation from the surface. A similar effect is apparent for hand-printed 0.25 mL spheres and boxes (**Figure S8A** and **S8C**). This raises the possibility of changing the heat capacity of the surroundings to modulate the  $\Delta T$  achieved, see below.

### 2.3. Hyperthermic responses of patterned magnetic gels.

As the typical volume of the magnetic gel component of a 3D printed structure for applications will typically be less than 0.1 mL, the observations in the previous section suggest a marginal  $\Delta T$  c.1 °C would be expected using MNF-G-210 in the open system, which is below the target range and close to background. The reduced surface area of fine-printed lines or structures might reduce this further. The MNF concentration was therefore increased ~12-fold to produce MNF-G-2500 inks. An in-house built 3D printer (details in Experimental) was used to extrude 5 x 5 and 10 x 10 square grids (with intended size 1.5 cm x 1.5 cm) of MNF-G-2500 (**Figure 5A, B**), that exhibited high-fidelity, comparable to MNF-G-210 upon minimal optimisation, suggesting minimal rheological changes at this concentration. The direction of printing nozzle is shown in **Figure S9**, and the G.codes are provided in Supporting Information (GS1 and GS2). The materials retained similar homogeneity with no visible aggregates apparent on optical inspection. For imaging heat dissipation in the printed structures we used a cooled camera (A6735sc) enabling higher resolution imaging and more accurate recording of temperature. In the open system, on average for both of the

printed grids we recorded temperature jumps  $\Delta T_{600} \geq 6$  °C, within range as expected, significantly higher than for poured MNF-G-210 of a comparable 0.1 mL total volume, which is very encouraging. ‘Empty’ areas inside the grids’ squares heated up on average by  $\sim 2$  °C, whereas the points outside of the grids increased by  $\sim 1$  °C, again indicating some diffusive heat flow from the magnetic patterned gel to spaces surrounding it. Similarly, for grids printed with purposely interrupted or ‘broken boxes’ the induced temperature jump could be moderated in a controlled fashion by reducing the continuity of the printed paths (**Figure S10**), which opens up other paths to spatial-heat control.

Thermography generally showed homogeneous heating over the continuous printing paths aside from hotspots in the thermal images for both of grids (**Figure 5C, D**) which are apparent within the temporal plots as a rapid ( $<10$  s) jump and early plateau. This feature corresponds to the end of the printing process, where the Z axis retracts and deposits additional material (**Figure S9**). Hence anomalies of this type can be eliminated by initiating and terminating printing off-feature.

To demonstrate spatially controlled thermally-induced heating paths on a micron scale thinner 5x5 grids were printed and a lens was used with the camera to enable *in situ* thermal imaging with spatial resolution of  $\sim 2$   $\mu\text{m}$  (**Figure 6**). Fine-printed lines of  $\sim 150$   $\mu\text{m}$  width with heat-induced homogeneously along the printed features are apparent (**Figure 6A**). On the other hand in 5x5 (thicker) grids, as described in **Figure 5A/Figure 6B**, there are clear trench and trough features indicative of the z-axis propagation during printing, at points too close to the surface of the Petri dish, and thus disrupting the gel during the print, leading to thicker lines of width  $\sim 300$   $\mu\text{m}$ . This process leads to formation of diffusive heating pathways linked to varied local topography of each line, a feature only apparent with highest-resolution

imaging available to us. We also note that the AMF response of the 10x10 thick grid (**Figure 6c**) resembles that of 5x5 grid with homogeneous surface thermography.

## 2.4. Demonstration of responsive dye delivery from printed features

For any cell culture or biomedical applications molecules of interest are released into aqueous environments, typically in extracellular matrix/tissues *in vivo*. We therefore printed three 3 mm x 3 mm side squares of MNF-G-2500 on a glass substrate, as before, partially embedded, and fully embedded in 40 w/v% Pluronic F127 of estimated similar matrix diffusion coefficient to that of MNF-G-2500. Again, we recorded temperature jumps  $\Delta T_{600}$  for all cases, giving average  $\Delta T_{600}$  values of 1.5, 3.0 and 4.5 °C, for glass and partially in-F127 and fully in-F127 substrates, respectively (**Figure 7A-C**). Assuming F127 hydrogel consists mainly of water with the heat capacity of which is  $4.186 \text{ J g}^{-1} \text{ K}^{-1}$ , the matrix surrounding MNF-G-2500 will act as insulator and allow more heat to be retained, compared to  $\sim 1 \text{ J g}^{-1} \text{ K}^{-1}$  for air, and  $\sim 0.84 \text{ J g}^{-1} \text{ K}^{-1}$  for a glass, in a ‘fully’ open system (compare Figure 7C to B to A). This result is encouraging as it confirms that the target  $\Delta T$  values noted above are easily within range (and can be adjusted across that range through the concentration).

To demonstrate the advantages of localized heat induction in printed magnetic hydrogels we loaded methylene blue at a concentration of  $0.1 \text{ mg mL}^{-1}$  into MNF-G-714, and investigated dye diffusion by optical imaging with and without the application of AMF over 10 & 20 mins irradiation (**Figure 7D-E**). The dye displacement (measured using ImageJ/Fiji,<sup>[48]</sup> see materials and methods) was found to be significantly ( $P < 0.05$ ) higher for the prints with irradiation at 20 mins irradiation time, as compared to non-irradiated case at the same time (**Figure 7D**), demonstrating the advantages of temperature-increased diffusion through AMF magnetic hyperthermia in fine print. To further validate this idea, we also printed three boxes in

a diagonal relative orientation and a 2 x 2 box and repeated these measurements (**Figure S11**). In all cases, 20 mins irradiation time revealed significantly higher dye displacements as compared to conventional diffusion without any AMF irradiation. This simple demonstration provides a basis for further investigations of controlled releases from magnetically-responsive printed features with enhanced control for future automated/controlled regenerative and cell culture applications, for instance by incorporating thermally responsive polymers as patterned layers within the printed structure.

### 3. Conclusion

In summary, a simple magnetic hydrogel nanocomposite that efficiently induces heat on AMF exposure is presented. The model ink is a stable dispersion of magnetic iron oxide nanoflowers in Pluronic F127 with optimal rheological characteristics (rapid recovery upon increased strain/shear; full temperature cycle recoverability) for 3D printing of patterned hyperthermally responsive constructs. AMF exposure of the magnetic prints clarifies some key aspects relating performance to processing parameters (Fe concentration, hydrogel volume and surface area);

- (i) At fixed outer surface area or volume, the hyperthermic response of a printed feature increases with particle concentration;
- (ii) At fixed surface area and concentration the hyperthermic response increases with feature volume;
- (iii) At fixed volume and concentration the hyperthermic response increases as feature surface area increases;
- (iv) Changing heat capacity of the surroundings, *e.g.* embedding the magnetic gel inside non-magnetic gel, decreases heat losses improving response and making target temperature jumps easily accessible within the concentration range used.



These observations show that for high resolution printed magnetic structures of different dimension the particle concentrations required to provide defined heat jumps within the target range can be predicted, opening up a range of tissue engineering applications. The applicability of the approach is shown using AMF-induced methylene blue dye release from fine printed structures as an example. This study will contribute to a greater understanding of formulation and function of magnetic hydrogels, which are of already of significant interest as next-generation responsive supports for tissue engineering,<sup>[49, 50]</sup> and for which the nascent promise of spatial patterning by 3D printing is now becoming apparent.

#### 4. Experimental Section

*Magnetic nanoflower (MNF) preparation:* Synthesis of iron oxide nanoflowers was based on the thermal decomposition of iron chloride precursors in organic media and adapted from Hugounenq *et al.*<sup>[38]</sup>. Briefly, in a typical preparation 0.541 g of Iron (III) chloride hexahydrate, 0.199 g of Iron (II) chloride tetrahydrate and 0.32 g of sodium hydroxide were dissolved in a 37.1 mL (1:1 by volume) mixture of DEG and NMDEA in a 100 mL round bottom flask. The resulting mixture was magnetically stirred for 3 hrs. Then, the temperature was increased to 220°C at 5°C/min by placing the round bottom flask in temperature-controlled heating mantle. The suspension was heated with magnetic stirring for 12 hrs, and then allowed to cool to room temperature. The black sediments were separated magnetically and washed with 10 mL portions a mixture (1:1 by volume) of ethanol and ethyl acetate 3 times to remove impurities. Possible iron hydroxides were removed by treatment with 10 mL 10% nitric acid for 15 mins. 4.125 g sample of iron (III) nitrate nonahydrate was then dissolved in 10 mL of water and added to the nanoparticle suspension. The resulting mixture was heated to 80 °C for 45 mins to ensure complete oxidation of the nanoparticles, to  $\gamma$ -Fe<sub>2</sub>O<sub>3</sub>. After

another treatment with 10% nitric acid, the suspension was washed twice with acetone and diethyl ether and re-dispersed in desired amount of water.

*Dynamic light scattering (DLS):* Experiments were performed at 25°C on a Malvern NanoZS (Malvern Instruments, Malvern UK) instrument, which uses a detection angle of 173°, and a 3 mW He-Ne laser operating at a wavelength of 633 nm. The Z-Average (mean hydrodynamic) diameter,  $d_{\text{hyd}}$ , and the polydispersity index (PDI) values were obtained from analysis of the correlation functions by cumulants analysis using the Dispersion Technology software (v. 4.10, Malvern Instruments; Worcestershire, U.K.).

*Transmission electron microscopy (TEM):* Images were acquired on a Hitachi transmission electron microscope at an accelerating voltage of 100kV. Samples were prepared by pipetting the aqueous suspensions of magnetic nanoflowers on to a Formvar coated copper grid and allowing drying naturally. Data analysis was using ImageJ and >100 particles were counted.

*Magnetic hydrogel preparation:* Hydrogels were prepared by dissolving 40% w/v of PF127 either in doubly distilled H<sub>2</sub>O or in the MNF suspension (at the required concentration) and homogenising by repeated centrifugation (5600 rcf for 5 mins) and cooling cycles under refrigeration (at 4°C for 24 hrs). Typically 2 cycles were sufficient. The samples are labelled here as, MNF-S-210 or MNF-G-210 for the suspensions and gels, respectively, at 210 mM final Fe concentration.

*Scanning electron microscopy:* Prior to imaging, the hydrogels were flash-frozen in liquid nitrogen and lyophilized to form freeze-dried solids. These were carefully cut into small discs that were coated with a 10 nm layer of gold using Emitech K575X Peltier cooled sputter coater by Quorum Technologies, using a 30 mA sputter current for 15 secs. These samples were then imaged using Hitachi TM4000 plus scanning

electron microscope. Energy dispersive X-ray spectroscopy (EDX) was performed using an Oxford Instruments SDD detector.

*Oscillatory rheology:* The oscillatory rheology was performed on Physica MCR301 rheometer from Anton Paar. Parallel plate geometry with a 25 mm diameter top plate and 0.5 mm gap was used. About 200  $\mu\text{L}$  of sample was placed on the bottom plate using a spatula, and subsequently the top rheometer plate was slowly lowered to minimize hydrogel disruption. LVR regions were defined using amplitude sweeps performed from 0.01% to 100% strain at  $f = 1$  Hz at 21  $^{\circ}\text{C}$ . Frequency scans were then performed from 0.1 to 15 Hz at 0.2% strain at 21  $^{\circ}\text{C}$ , within the linear viscoelastic regime of all the samples. Hydrogel recovery tests were performed in time mode by initially subjecting samples to 0.2% strain at  $f = 1$  Hz for 30 secs. Strain was then increased to 100% and maintained for 10 s. Recovery was then monitored for 120 seconds by switching the strain back to 0.2%. Temperature sweeps were performed from room temperature 20  $^{\circ}\text{C}$  to 45  $^{\circ}\text{C}$ , at  $f = 1$  Hz and strain 0.2%. To avoid sample evaporation, after the top plate was carefully lowered down to a desired gap, oil was carefully pipetted down around the sample enclosed between top and bottom plates, and a humidity control hood was used. The heating rate was set to +1  $^{\circ}\text{C}/\text{min}$  and the cooling rate to -5  $^{\circ}\text{C}/\text{min}$ . All measurements were repeated at least three times.

*Magnetic hyperthermia:* Measurements on bulk homogeneous samples were carried out using a NanoTherics NAN201003 MagneTherm<sup>TM</sup> AC field generator (NanoTherics Ltd.; Newcastle-under-Lyme, United Kingdom). The system allows measurement of temperature vs time via a non-metallic OP-Sens optical thermometer to avoid eddy currents. Typically 1 mL of sample was transferred into a plastic cylindrical shape 2 mL Eppendorf tube with a whole on a cup that fits well the optical thermometer probe. The sample was placed in a thermally insulating polystyrene sample holder to maintain close-to-adiabatic conditions. The sample temperature was

measured by Fibre Optic Probe (Opsens Ltd., Canada), typically fitted 0.25 mm below the surface of a sample. The temperature of the sample was equilibrated in the instrument before the desired field was applied. Unless otherwise noted, measurements were carried out at a frequency of 535 kHz and magnetic field strength of 24 mT. These will be referred to as ‘closed system’ measurements. The errors indicated for SAR determinations ( $309 \pm 26$  and  $43 \pm 6$  W.g<sup>-1</sup> for suspensions and gels, respectively) are *c.*10%. These reflect the average/std dev of three independent SAR determinations on three repeat formulations, *i.e.* 9 values in each case. For each SAR determination the initial slope is taken as the average of the linear fitting term from three temperature cycles shown for instance in Figure 1D, which has uncertainty *c.*2-3%. The error in determining concentration of Fe using AAS is estimated to also be *c.*2-3%. Hence the batch to batch variation for suspensions and gels is acceptable for the purposes of generating reproducible temperature jumps in magnetic gels.

*In situ thermal imaging during alternating magnetic field (LC-AMF) irradiation:*

Measurements on composite gels were carried out on a Live Cell–Alternating Magnetic Field (LC-AMF<sup>TM</sup>) module connected to a NanoTherics NAN201003 MagneTherm<sup>TM</sup> system, see Fig. S4, which enables RF irradiation of a sample placed in a standard Petri dish. Measurements were carried out at a frequency of 642 kHz and magnetic field strength of 16 mT. Thermal imaging was performed using a Flir A655sc thermal camera, and a Flir A6735sc cooled thermal camera kindly provided by Butler Technologies. The camera was aligned to view hydrogels carefully placed in 35 mm glass Petri dishes, unless otherwise stated. Recordings were made for 10 mins and the AMF was turned on immediately after the recording started. Each 10 mins recording consists of; 3750 frames at 6.25 Hz for the A655sc camera, or; 4500 frames at 7.5 Hz for the A6735sc. The resolution of the A655sc camera is  $\sim 170$   $\mu$ m (pixel

size) increasing to  $\sim 60\ \mu\text{m}$  with the additional close-up lens, and that of the A6735sc is  $\sim 6\ \mu\text{m}$ , increasing to  $\sim 2\ \mu\text{m}$  with the additional lens. The whole setup was placed in a temperature stabilised room with the camera and AMF system shielded to minimise IR reflections and temperature fluctuations during imaging. These will be referred to as ‘open system’ measurements. Both thermal cameras detect temperature differences down to  $<30\ \text{mK}$ , even at longer working distance. Both cameras feature internal calibrations, which were run prior capturing each dataset. The internal calibrations, or Non Uniformity Corrections, accord to ISO9001:2008 as detailed at <https://www.flir.com/support-center/Instruments/service/calibration-technical-data/>.

*3D printing:* Hydrogels were stored, as liquids, at  $4^\circ\text{C}$ . In preparation for printing they were removed from the fridge and immediately transferred to the syringe and the returned to  $4^\circ\text{C}$  for 5 mins to remove any bubbles, and finally rested at  $18^\circ\text{C}$  for 10 mins prior to printing. A Naiad V1 3D bioprinter, developed in-house by EGR and BJR in partnership with Naiad 3D printing Ltd, was used to perform the grid prints. Briefly, the 3D bioprinter enables syringe-based extrusion via a pressure valve and dedicated software. The temperature-controlled syringe head is attached to a robotic gantry stage with 2-axis motors. In this system, air pressure is applied on a loaded plastic tapered dispensing needles (Somerset Solders Ltd) pushing the material down a nozzle (30 gauge Luer Lock dispensing tips, Fisnar, Europe) that can be changed depending on ink viscosity or required printing parameters (inner nozzle diameters of 0.58, 0.84, 1.20, and 1.50 mm). For the grid prints, the pressure was kept constant as 2 Bar (hydrogel extrusion =  $1\ \text{mm}^3\cdot\text{s}^{-1}$ ) using a  $150\ \mu\text{m}$  nozzle positioned at  $150\ \mu\text{m}$  from the printing platform. Printing was performed at a constant head velocity of  $25\ \text{mm}\cdot\text{s}^{-1}$ . The experiments were run at  $18^\circ\text{C}$  (room temperature). G.codes are available in supplementary information (GS1 and GS2).

*Imaging of methylene blue release:* Prior to 3D printing, MNF-G-714 hydrogels were prepared as above, except 0.1 mg mL<sup>-1</sup> methylene blue was additionally loaded as an exemplar cargo molecule for release. For this experiment printing took place on a bed of Pluronic, to serve both as an insulator for the gel (as discussed in the main text), and to provide a hydrated hydrogel environment mimicking that of cell culture/tissue. To avoid significant mismatch of diffusivity between MNF-G-714 and the model, we used F127 at the same concentration (40 w/v%). The samples were irradiated for 1200 seconds with images taken at 0, 600, and 1200 seconds using an Olympus BX52 microscope. The full dye-inclusive width (FW) was measured in ImageJ/Fiji at three time points.<sup>[48]</sup> Firstly, the same colour threshold was set for all images to maintain the sufficient contrast in all cases for the following steps. To incorporate the print and dye into one ‘feature’ for quantification, the edges of prints (dye) were then maximised and made binary. Line profiles perpendicular to the direction of printing were then drawn and dye displacement calculated for the two time points as; FW<sub>600</sub>-FW<sub>0</sub> or FW<sub>1200</sub>-FW<sub>0</sub>, where the index refers to the irradiation LC-AMF time in seconds after which the image was recorded. For a single printed box (main text), 4 sides were used (n=4), whereas for other structures (**Figure S11**), 8 sides were used (n=8). All data is represented as mean ± standard deviation. The statistical significance was calculated using unpaired t-test in Graph Pad Prism v7.0. Statistical significance was considered at 95% confidence interval at P<0.05 (denoted as \*).

*Optical Imaging of Prints/Hydrogels:* Images of Prints or hydrogels were taken under either (i) standard smartphone camera (ii) Olympus BX52 microscope or (iii) StereoDiscovery V20 Carl Zeiss Microscope.

**Supporting Information**

Supporting Information is available from the Wiley Online Library or from the author.

**Acknowledgements**

The authors acknowledge support from Science Foundation Ireland (16/IA/4584, 13/IA/1840, and 13/TIDA/B2701) and Enterprise Ireland (CF-2016-0389-P). We thank the Butler Technologies and Mr. David Doyle for allowing us to use A6735sc thermal camera for the purpose of these measurements. We would also like to acknowledge Kevin M<sup>c</sup>Carthy and Mark M<sup>c</sup>Donagh for supporting 3D printing experiments and Sabine Harrison (School of Agriculture and Food Science, UCD) for supporting access to the rheometer.

Received: ((will be filled in by the editorial staff))

Revised: ((will be filled in by the editorial staff))

Published online: ((will be filled in by the editorial staff))

**References**

- [1] S. Joo, J. Yeon Kim, E. Lee, N. Hong, W. Sun, Y. Nam, Scientific Reports 2015, 5, 13043.
- [2] N. Gjorevski, N. Sachs, A. Manfrin, S. Giger, M. E. Bragina, P. Ordóñez-Morán, H. Clevers, M. P. Lutolf, Nature 2016, 539, 560.
- [3] P. Lu, V. M. Weaver, Z. Werb, Journal of Cell Biology 2012, 196, 395.
- [4] J. H. Lee, Biomaterials Research 2018, 22, 27.
- [5] S. L. Pedersen, T. H. Huynh, P. Pöschko, A. S. Fruergaard, M. T. Jarlstad Olesen, Y. Chen, H. Birkedal, G. Subbiahdoss, E. Reimhult, J. Thøgersen, A. N. Zelikin, ACS Nano 2020.

- [6] T. Billiet, M. Vandenhaute, J. Schelfhout, S. Van Vlierberghe, P. Dubruel, *Biomaterials* 2012, 33, 6020.
- [7] J. Patterson, M. M. Martino, J. A. Hubbell, *Materials Today* 2010, 13, 14.
- [8] W. Zhu, K. R. Tringale, S. A. Woller, S. You, S. Johnson, H. Shen, J. Schimelman, M. Whitney, J. Steinauer, W. Xu, T. L. Yaksh, Q. T. Nguyen, S. Chen, *Materials Today* 2018, 21, 951.
- [9] W. Zhu, X. Qu, J. Zhu, X. Ma, S. Patel, J. Liu, P. Wang, C. S. E. Lai, M. Gou, Y. Xu, K. Zhang, S. Chen, *Biomaterials* 2017, 124, 106.
- [10] P. Wang, D. Berry, A. Moran, F. He, T. Tam, L. Chen, S. Chen, *Advanced Healthcare Materials* 2019, 1900977;
- [11] W. He, M. Reaume, M. Hennenfent, B. P. Lee, R. Rajachar, *Biomaterials Science* 2020, 8, 3248.
- [12] S. Merino, C. Martín, K. Kostarelos, M. Prato, E. Vázquez, *ACS Nano* 2015, 9, 4686.
- [13] E. K. Fox, F. El Haddassi, J. Hierrezuelo, T. Ninjbadgar, J. K. Stolarczyk, J. Merlin, D. F. Brougham, *Small* 2018, 14.
- [14] J. K. Stolarczyk, A. Deak, D. F. Brougham, *Advanced Materials* 2016, 28, 5400.
- [15] S. van Rijt, P. Habibovic, *Journal of The Royal Society Interface* 2017, 14, 20170093.
- [16] J.-t. Jang, J. Lee, J. Seon, E. Ju, M. Kim, Y. I. Kim, M. G. Kim, Y. Takemura, A. S. Arbab, K. W. Kang, K. H. Park, S. H. Paek, S. Bae, *Advanced Materials* 2019, 31, 1806347.
- [17] B. T. Mai, P. B. Balakrishnan, M. J. Barthel, F. Piccardi, D. Niculaes, F. Marinaro, S. Fernandes, A. Curcio, H. Kakwere, G. Autret, R. Cingolani, F. Gazeau, T. Pellegrino, *ACS Applied Materials & Interfaces* 2019, 11, 5727.
- [18] F. Crippa, T. L. Moore, M. Mortato, C. Geers, L. Haeni, A. M. Hirt, B. Rothen-Rutishauser, A. Petri-Fink, *Journal of Magnetism and Magnetic Materials* 2017, 427, 212.
- [19] E. G. Fuller, H. Sun, R. D. Dhavalikar, M. Unni, G. M. Scheutz, B. S. Sumerlin, C. Rinaldi, *ACS Applied Polymer Materials* 2019, 1, 211



- [20] M. K. Jaiswal, M. De, S. S. Chou, S. Vasavada, R. Bleher, P. V. Prasad, D. Bahadur, V. P. Dravid, *ACS Applied Materials & Interfaces* 2014, 6, 6237.
- [21] N. A. Jalili, M. K. Jaiswal, C. W. Peak, L. M. Cross, A. K. Gaharwar, *Nanoscale* 2017, 9, 15379.
- [22] M. Antman-Passig, O. Shefi, *Nano Letters* 2016, 16, 2567
- [23] J. Kim, J. R. Staunton, K. Tanner, *Advanced Materials* 2016, 28, 132.
- [24] K. Hu, N. Zhou, Y. Li, S. Ma, Z. Guo, M. Cao, Q. Zhang, J. Sun, T. Zhang, N. Gu, *ACS Applied Materials & Interfaces* 2016, 8, 15113.
- [25] R. Tognato, A. R. Armiento, V. Bonfrate, R. Levato, J. Malda, M. Alini, D. Eglin, G. Giancane, T. Serra, *Advanced Functional Materials* 2019, 29, 1804647.
- [26] A. Augurio, P. Cortelletti, R. Tognato, A. Rios, R. Levato, J. Malda, M. Alini, D. Eglin, G. Giancane, A. Speghini, T. Serra, *Advanced Intelligent Systems* 2019, 1900105.
- [27] H. Ye, C. L. Randall, T. G. Leong, D. A. Slanac, E. K. Call, D. H. Gracias, *Angewandte Chemie International Edition* 2007, 46, 4991.
- [28] M. S. Yavuz, Y. Cheng, J. Chen, C. M. Cobley, Q. Zhang, M. Rycenga, J. Xie, C. Kim, K. H. Song, A. G. Schwartz, L. V. Wang, Y. Xia, *Nature Materials* 2009, 8, 935–939.
- [29] J. Park, C. Jin, S. Lee, J.-Y. Kim, H. Choi, *Advanced Healthcare Materials* 2019, 8, 1900213.
- [30] S. Aubert, M. Bezagu, A. C. Spivey, S. Arseniyadis, *Nature Reviews Chemistry* 2019, 3, 706; Y. V. Kalinin, A. Murali, D. H. Gracias, *RSC Advances* 2012, 2, 9707.
- [31] S. Dong, Y. Chen, L. Yu, K. Lin, X. Wang, *Advanced Functional Materials* 2020, 30, 1907071.
- [32] L. Lartigue, P. Hugounenq, D. Alloyeau, S. P. Clarke, M. Lévy, J.-C. Bacri, R. Bazzi, D. F. Brougham, C. Wilhelm, F. Gazeau, *ACS Nano* 2012, 6, 10935.
- [33] A. P. Herrera, C. Barrera, Y. Zayas, C. Rinaldi, *Journal of Colloid and Interface Science* 2010, 342, 540.

- [34] T. T. Emi, T. Barnes, E. Orton, A. Reisch, A. E. Tolouei, S. Z. M. Madani, S. M. Kennedy, *ACS Biomaterials Science & Engineering* 2018, 4, 2412.
- [35] M. Müller, J. Becher, M. Schnabelrauch, M. Zenobi-Wong, *Biofabrication* 2015, 7, 035006.
- [36] R. Suntornnond, E. Y. S. Tan, J. An, C. K. Chua, *Scientific Reports* 2017, 7, 16902; P. T. Smith, A. Basu, A. Saha, A. Nelson, *Polymer* 2018, 152, 42.
- [37] S. L. Vega, M. Y. Kwon, K. H. Song, C. Wang, R. L. Mauck, L. Han, J. A. Burdick, *Nature Communications* 2018, 9, 614.
- [38] P. Hugounenq, M. Levy, D. Alloyeau, L. Lartigue, E. Dubois, V. Cabuil, C. Ricolleau, S. Roux, C. Wilhelm, F. Gazeau, R. Bazzi, *The Journal of Physical Chemistry C* 2012, 116, 15702.
- [39] H. Arslan, A. Nojoomi, J. Jeon, K. Yum, *Advanced Science* 2019, 6, 1800703.
- [40] R. R. Wildeboer, P. Southern, Q. A. Pankhurst, *Journal of Physics D: Applied Physics* 2014, 47, 495003; A. Makridis, S. Curto, G. C. van Rhoon, T. Samaras, M. Angelakeris, *Journal of Physics D: Applied Physics* 2019, 52, 255001.
- [41] M. Avolio, A. Guerrini, F. Brero, C. Innocenti, C. Sangregorio, M. Cobianchi, M. Mariani, F. Orsini, P. Arosio, A. Lascialfari, *Journal of Magnetism and Magnetic Materials* 2019, 471, 504.
- [42] S. B. Campbell, M. Patenaude, T. Hoare, *Biomacromolecules* 2013, 14, 644.
- [43] M. Walker, I. Will, A. Pratt, V. Chechik, P. Genever, D. Ungar, *ACS Applied Nano Materials* 2020.
- [44] J. K. Wychowaniec, M. Iliut, M. Zhou, J. Moffat, M. A. Elsayy, W. A. Pinheiro, J. A. Hoyland, A. F. Miller, A. Vijayaraghavan, A. Saiani, *Biomacromolecules* 2018, 19, 2731.
- [45] E. Garreta, P. Prado, C. Tarantino, R. Oria, L. Fanlo, E. Martí, D. Zalvidea, X. Trepát, P. Roca-Cusachs, A. Gavaldà-Navarro, L. Cozzuto, J. M. Campistol, J. C. Izpisua Belmonte, C. Hurtado del Pozo, N. Montserrat, *Nature Materials* 2019, 18, 397.

- [46] Thermosets: Structure, Properties and Applications 2012, 1.
- [47] T. L. Place, F. E. Domann, A. J. Case, Free Radical Biology and Medicine 2017, 113, 311.
- [48] J. Schindelin, I. Arganda-Carreras, E. Frise, V. Kaynig, M. Longair, T. Pietzsch, S. Preibisch, C. Rueden, S. Saalfeld, B. Schmid, J.-Y. Tinevez, D. J. White, V. Hartenstein, K. Eliceiri, P. Tomancak, A. Cardona, Nature Methods 2012, 9, 676.
- [49] J. Liao, H. Huang, Biomacromolecules 2020, 21, 7, 2574–2594.
- [50] Z. Liu, J. Liu, X. Cui, X. Wang, L. Zhang, P. Tang, Frontiers in Chemistry 2020, 8, 124.

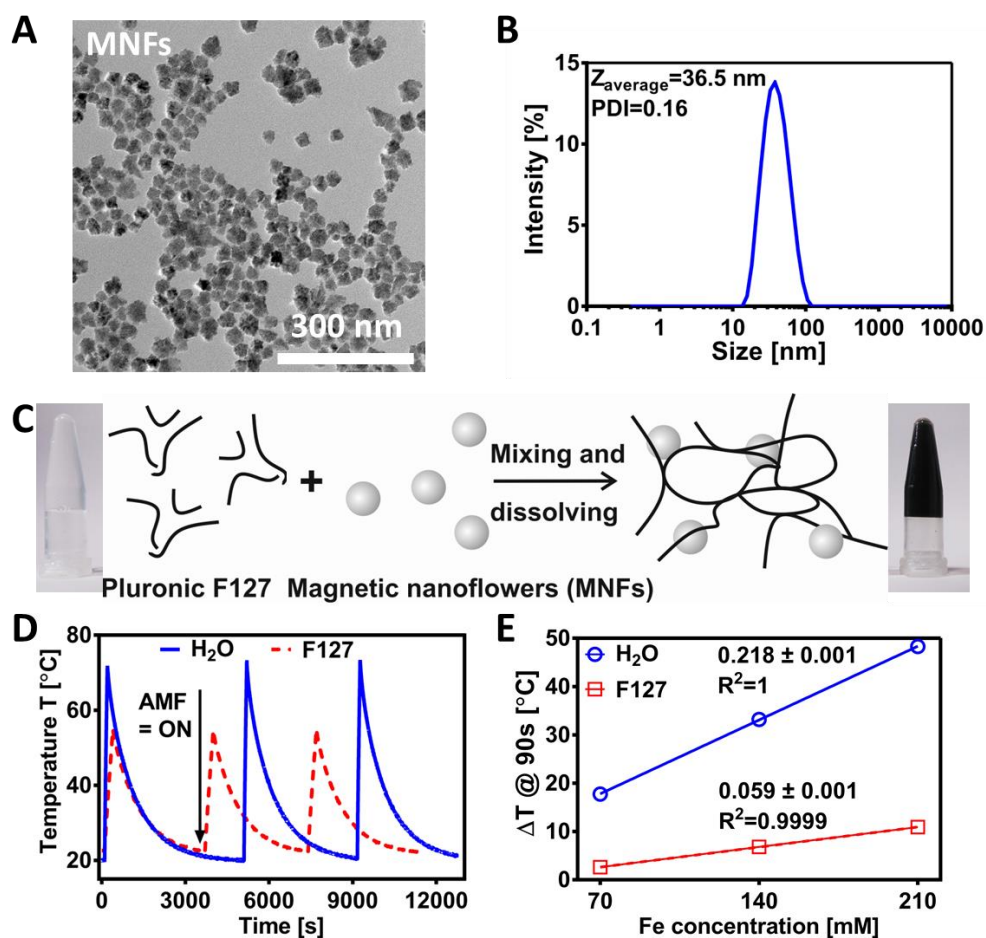


**Figure 1.** (A) A representative TEM image of magnetic nanoflowers (MNFs)  $d_{\text{TEM}} = 20.7 \pm 2.5 \text{ nm}$ ; (B) DLS intensity size distribution of an aqueous as-prepared MNF suspension with  $d_{\text{hyd}} 36.5 \text{ nm}$ ,  $\text{PDI} 0.16$ ; (C) Scheme depicting the preparation of F127-MNF magnetic hydrogels. The photographs on the left and right show inverted vials of 40 w/v% Pluronic F127 and 40 w/v% F127 with 210 mM Fe; (D) Cycled magnetic hyperthermia response (open system) of MNFs dispersed in  $\text{H}_2\text{O}$  at  $[\text{Fe}] 210 \text{ mM}$  (MNF-S-210) and magnetic F127 hydrogel with  $[\text{Fe}] = 210 \text{ mM}$  (MNF-G-210); (E) Extracted temperature jump values after 90 s of AC field irradiation time ( $\Delta T_{90}$ ) for MNF suspensions and 40 w/v% F127 hydrogels with different Fe loading,  $n = 3$ , error bars are included but are smaller than the data markers. The straight line fits obtained (even for three concentrations) demonstrate unchanging ‘SAR’ values of

$309 \pm 26$  and  $43 \pm 6$  W.g<sup>-1</sup> for suspensions and gels, respectively, across this concentration range.

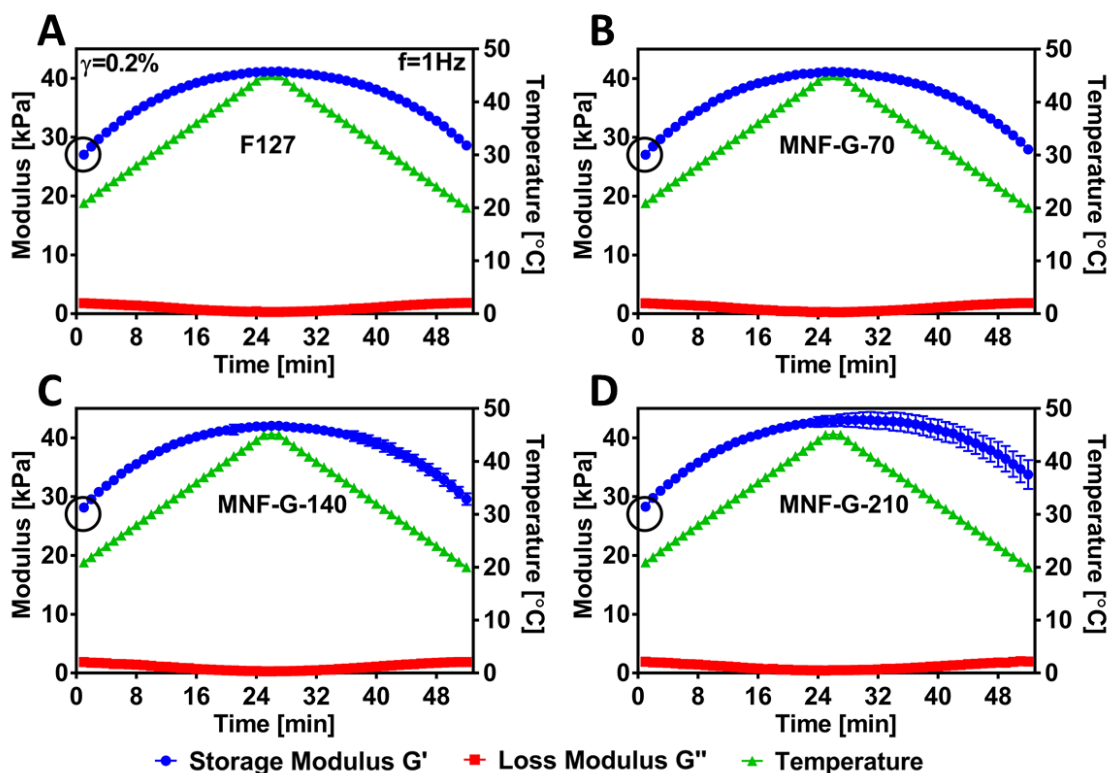


**Figure 2.** Temperature sweeps at  $f = 1$  Hz,  $\gamma = 0.2\%$  strain for; (A) 40 w/v% F127; (B) MNF-G-70; (C) MNF-G-140, and; (D) MNF-G-210.  $n = 2$  in all cases (measurements were repeated for two samples from the same batch) and the std deviations/error bars are a measure of the span of the data. The error bars are smaller than the data mark size, except in D. The initial  $G'$  values at 20 °C are marked with a circle, illustrating similar  $G'$  for all gels under these conditions (see also Figures S2-S3).

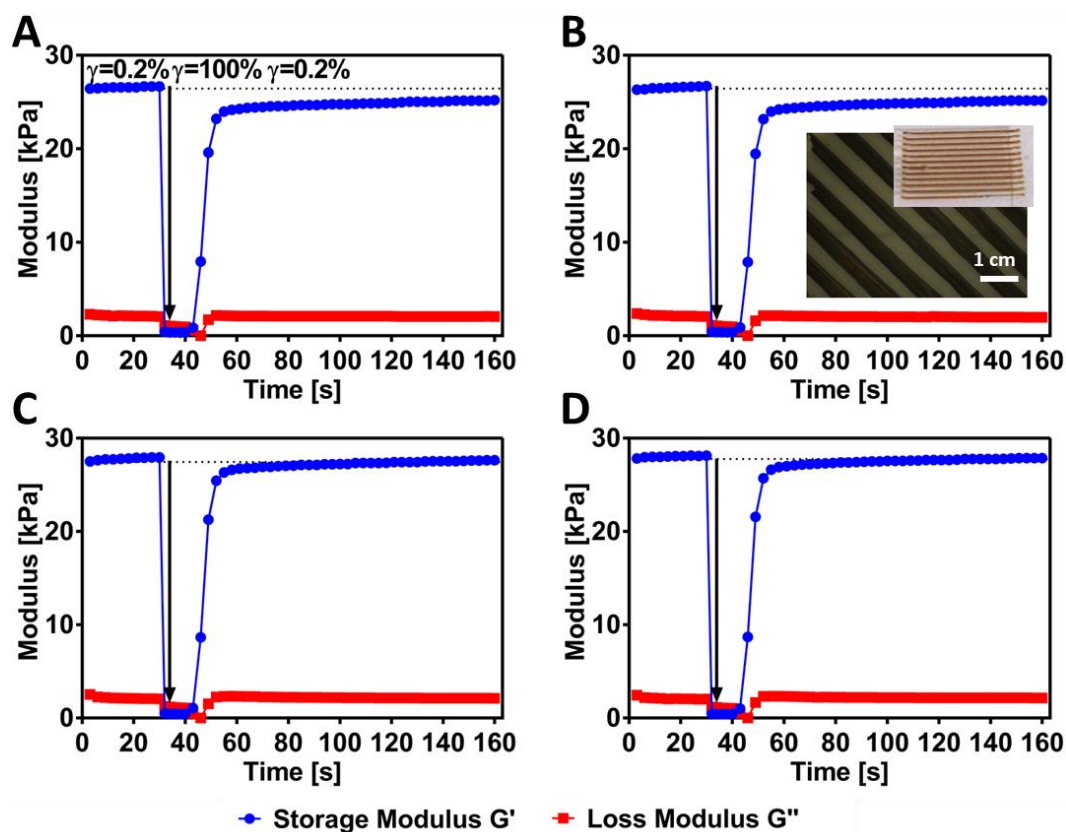


**Figure 3.** Rheological recovery of the formulations at 21 °C, measured at  $f = 1$  Hz, with strain change from  $\gamma = 0.2$  to 100% simulating the printing process for; (A) 40 w/v% F127; (B) MNF-G-70; (C) MNF-G-140; (D) MNF-G-210. Images of lines printed using MNF-G-70 are shown as an inset to B demonstrating excellent fidelity after printing, which is observed across the concentration range. Error bars representing the standard deviations are included for panels A-D,  $n = 3$  corresponding to separate measurements for 3 samples from the same batch. The bars are smaller than the data mark size.

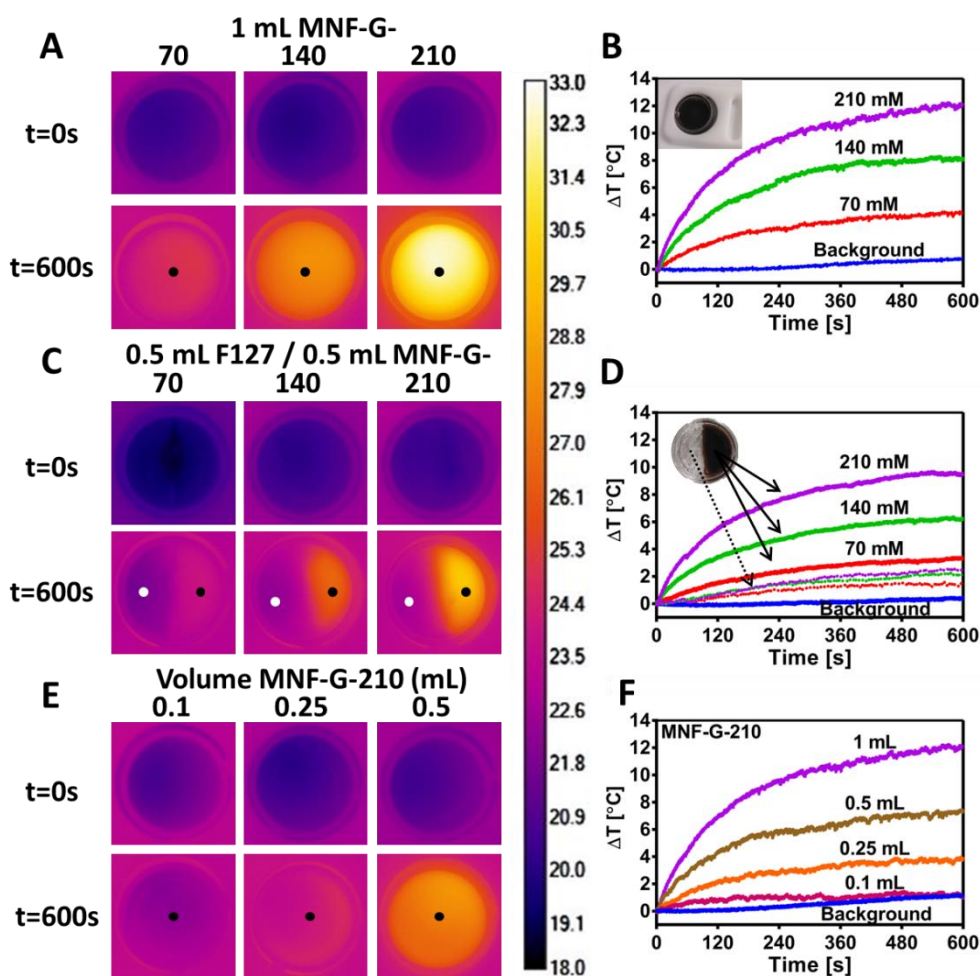


**Figure 4.** Time resolved in-situ thermography of ‘open system’ AMF stimulation of; (A) 1 mL of MNF-G-70, -140 and -210; (C) 0.5 mL of F127 and 0.5 mL of MNF-G-70, -140 and -210 poured side by side, and; (E) 0.1, 0.25 and 0.5 mL of MNF-G-210. Panels (B), (D) and (F) show the change in temperature ( $\Delta T$ ) as a function of irradiation time at the position of greatest temperature increase (identified by black dots) for (A), (C) and (E), respectively. Thermography data was recorded using the A655sc thermal camera (without lens) with spatial resolution  $\sim 170 \mu\text{m}$ . The colours in B and D code different concentrations, whereas colours in F code different gel volumes. Note the purple line in F represents the same data as the purple curve as in B. The heating recorded at the white dots in C is included in D as dashed lines of the same colour for a given concentration. The background is taken at a position outside

the AC field (see Figure S4). All measurements were initiated at  $\sim 18$ - $19$  °C. A single colour scale is used for all thermal images in the Figure.

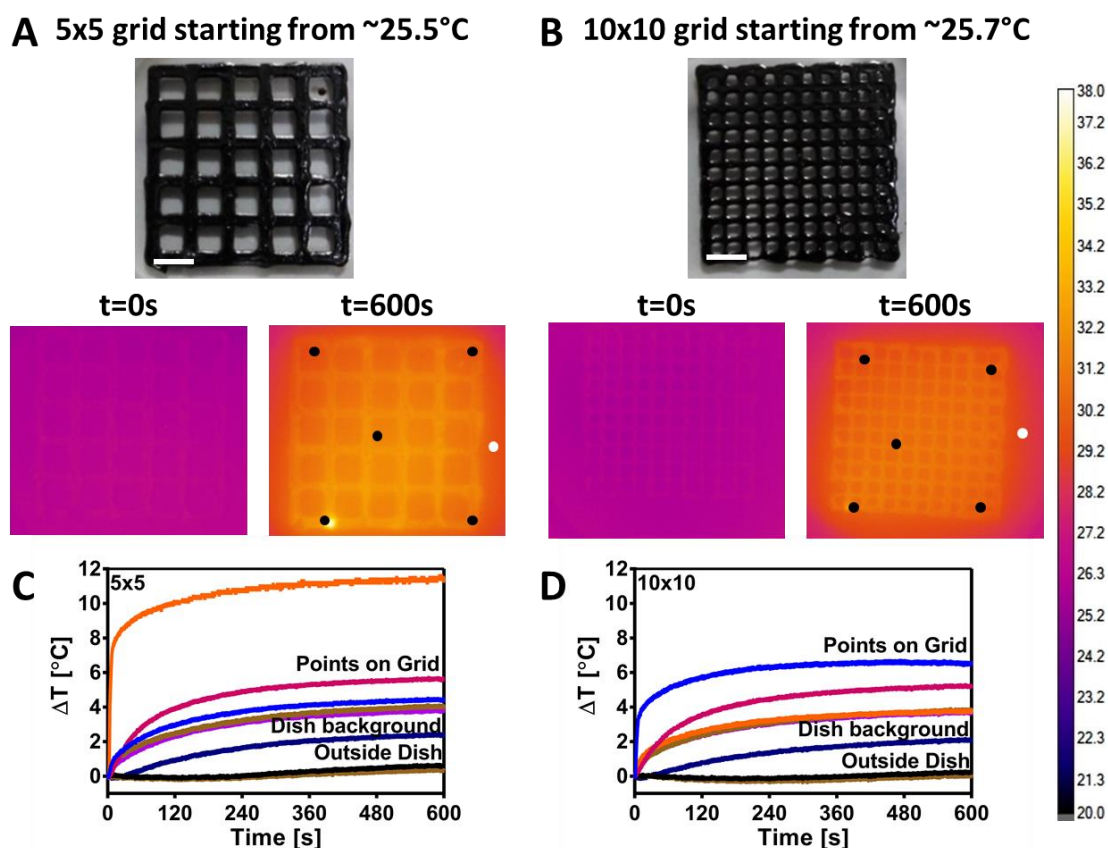


**Figure 5.** 3D printing scheme of (A) 5 x 5 grid and (B) 10 x 10 grid from MNF-G-2500 using the A6735sc camera with spatial resolution  $\sim 6$   $\mu\text{m}$  (pixel size). Note that a common thermal scale is provided for A and B. (C) and (D) Temporal change in temperature ( $\Delta T$ ) plots over 600 seconds irradiation time for A and B, respectively. The white scale bar in the optical image indicates 5 mm. The white dot represents the dish background. For the outside dish background 2 other points were selected outside of the image area shown. Note the highest heating point in C is the point at which printing was finished (details in main text). Different colours represent different cursors position on the grid (as indicated by black dots on thermal image). Illustrative



videos of the thermal response are provided in supporting information (Movies MS1 and MS2).

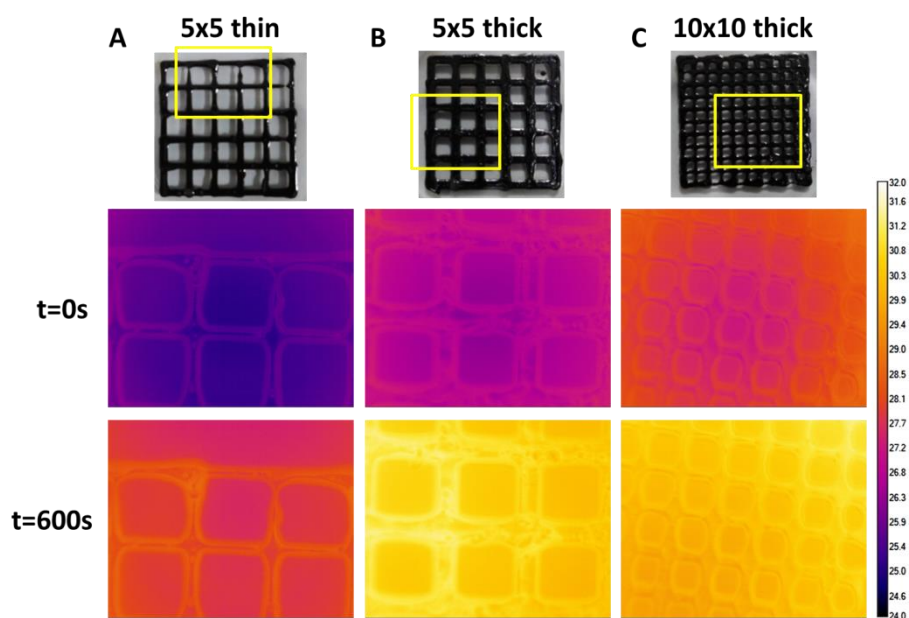


**Figure 6.** 3D printing scheme of (A) 5 x 5 thin, (B) 5 x 5 thick, and (C) 10 x 10 thick grid from MNF-G-2500 with associated heat maps from the rectangular parts drawn on printed grids. The A6735sc camera was used with an additional lens to further increase spatial resolution down to  $\sim 2 \mu\text{m}$  per pixel.

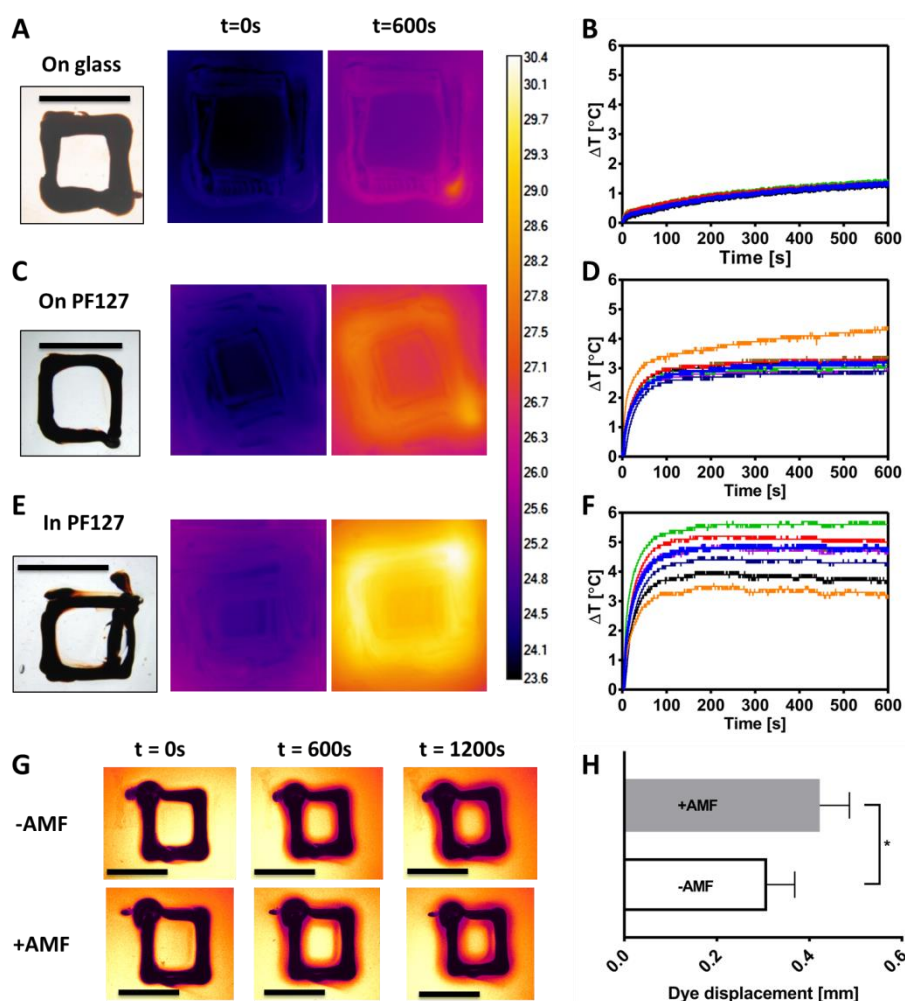
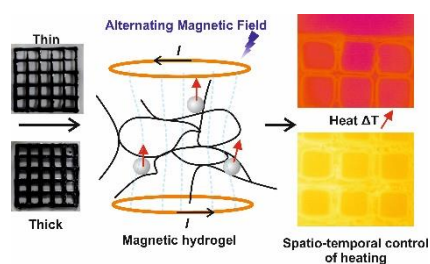


**Figure 7.** Temporal change in temperature ( $\Delta T$ ) plots over 600 seconds irradiation time for a single MNF-G-2500 box printed (A-B) on glass; (C-D) approx. 0.5 mm and (E-F) approx. 3 mm below surface of non-magnetic F127 Pluronic hydrogels. Curves across multiple randomly chosen points on the printed grid are represented in different colors. The black scale bar in the optical image indicates 3 mm. A single colour scale is used for all thermal images in the Figure. (G) Optical measurements of printed single box MNF-G-714 grids (scale bars = 3 mm) with  $0.1 \text{ mg mL}^{-1}$  methylene blue with and without AMF for  $t = 0, 600$  and  $1200$  s. (H) Dye displacement represented from the optical images obtained in (G). Measurements were taken on middle part of 4 sides ( $n=4$ ) and statistical significance was calculated between +AMF and -AMF samples at  $1200$  s with 95% confidence interval (using unpaired t-test in Graph Pad Prism 7.0). \* denotes  $P < 0.05$ .

Spatio-temporally specified heating within printed magnetic-nanocomposite materials is a novel approach to advanced responsive systems. Selective encoding of spatiotemporally controlled heating response in 3D printed magnetic hydrogels under alternating magnetic field stimulus is demonstrated here, with applications in soft robotics, drug delivery and regenerative medicine. The performance-design rules identified establish the possibility of sufficient temperature responses on length and time scales relevant to tissue engineering.

P. Monks, J. K. Wychowaniec, E. M<sup>c</sup>Kiernan, S. Clerkin, J. Crean, B. J. Rodriguez, E. G. Reynaud, A. Heise, D. Brougham<sup>\*</sup>

### Spatiotemporally resolved heat dissipation in 3D patterned magnetically responsive hydrogels



## Supporting Information

**Spatiotemporally resolved heat dissipation in 3D patterned magnetically responsive hydrogels**

*Patricia Monks, Jacek K. Wychowaniec, Eoin M<sup>c</sup>Kiernan, Shane Clerkin, John Crean, Brian J. Rodriguez, Emmanuel G. Reynaud, Andreas Heise, Dermot Brougham\**

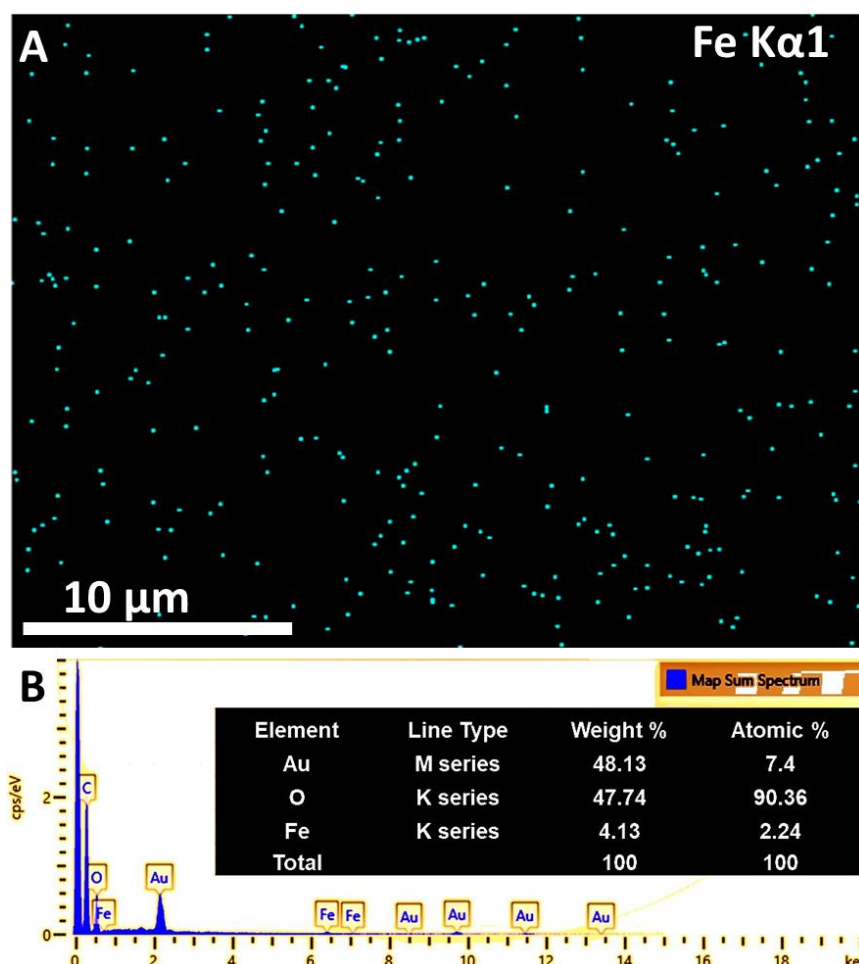


**Figure S1.** (A) Spatial energy dispersive X-ray spectroscopy of the scanning electron microscopy part of a 40 w/v% F127, 70 mM Fe freeze-dried magnetic hydrogel with (B) associated elemental distribution map and averaged content.

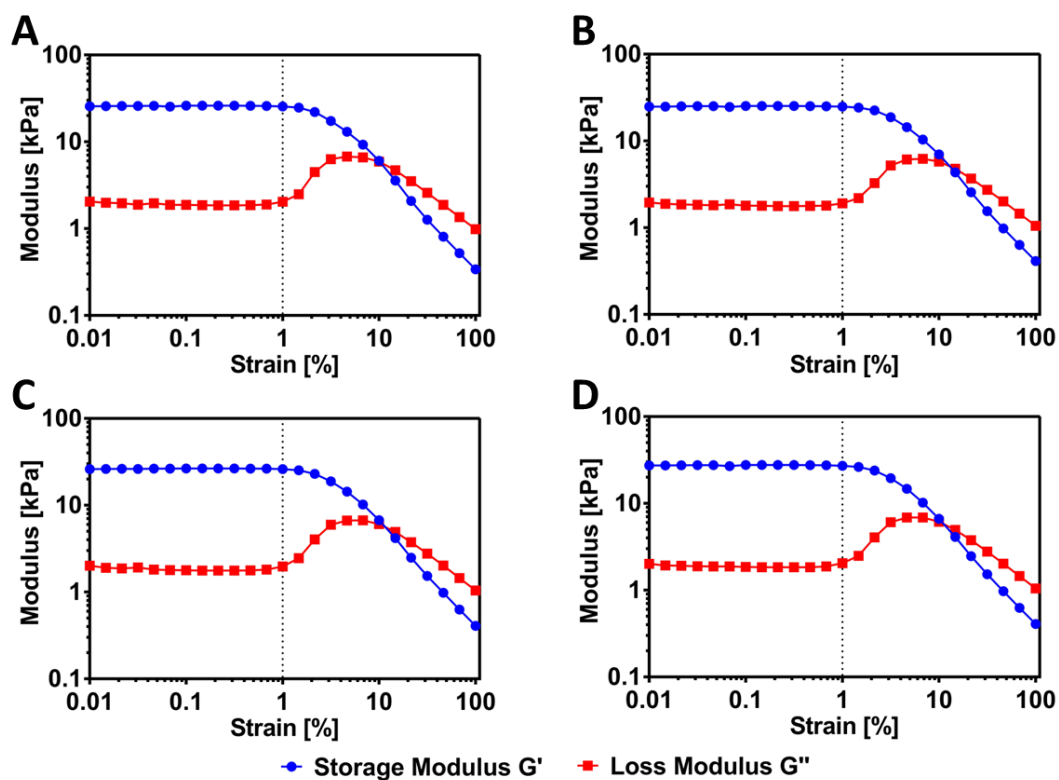


**Figure S2.** Amplitude sweeps at 1 Hz and at 21 °C showing linear viscoelastic region (LVR) of: (A) 40 w/v% F127, (B) MNF-G-70, (C) MNF-G-140, (D) MNF-G-210. (Note the explanation of hydrogel is given in main text, e.g. 40 w/v% F127-210 mM MNF magnetic hydrogels = MNF-G-210).

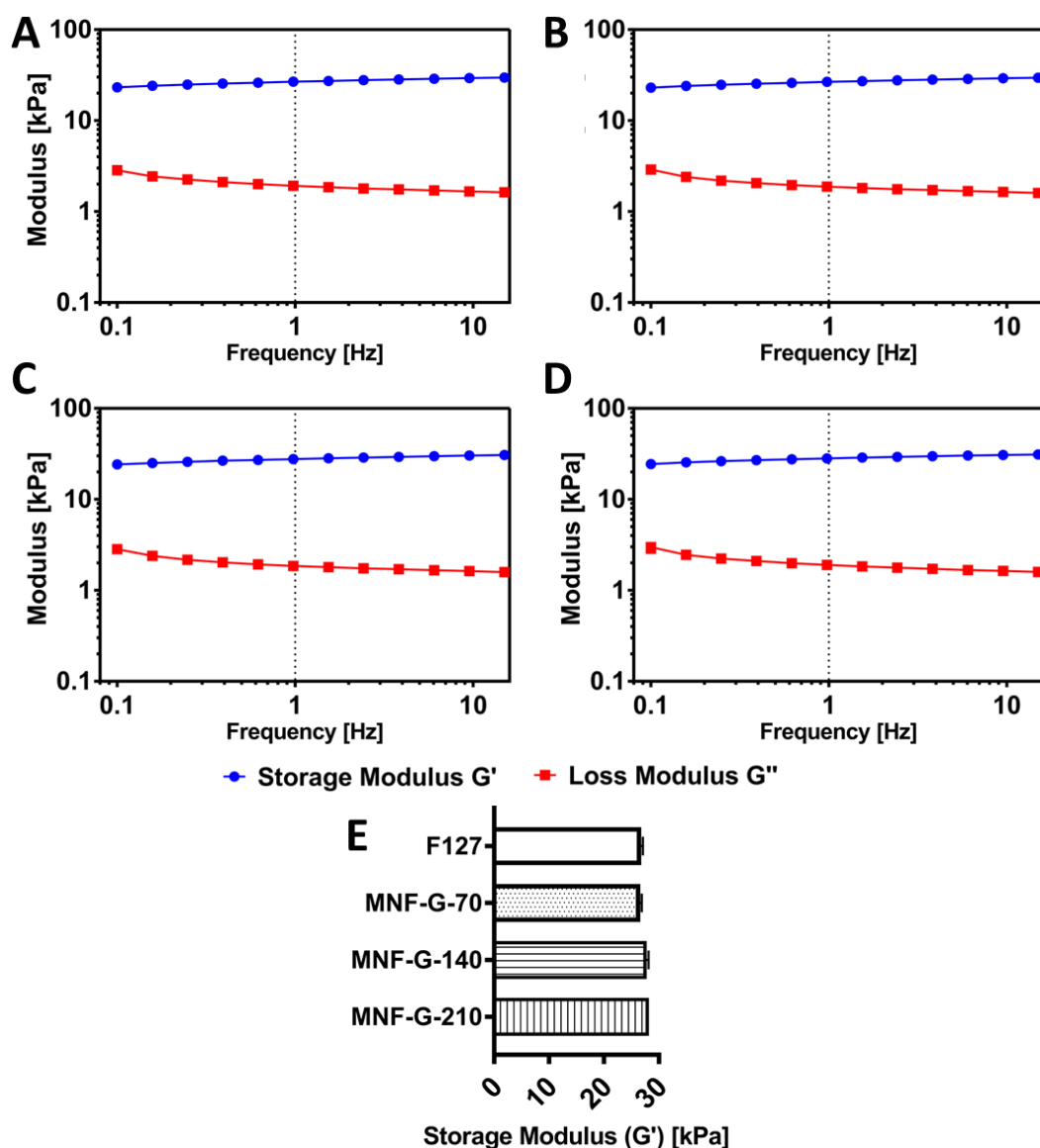


**Figure S3.** Frequency sweeps at  $\gamma=0.2$  % strain and at 21 °C of: (A) 40 w/v% F127, (B) MNF-G-70, (C) MNF-G-140, (D) MNF-G-210. (Note the explanation of hydrogel is given in main text, e.g. 40 w/v% F127-210 mM MNF magnetic hydrogels = MNF-G-210). (E) Average storage modulus of all hydrogels taken from frequency sweeps at  $f = 1$  Hz and  $\gamma = 0.2$  % strain ( $n=3$ ), note error bars (SD) are included in E for all 4 samples.

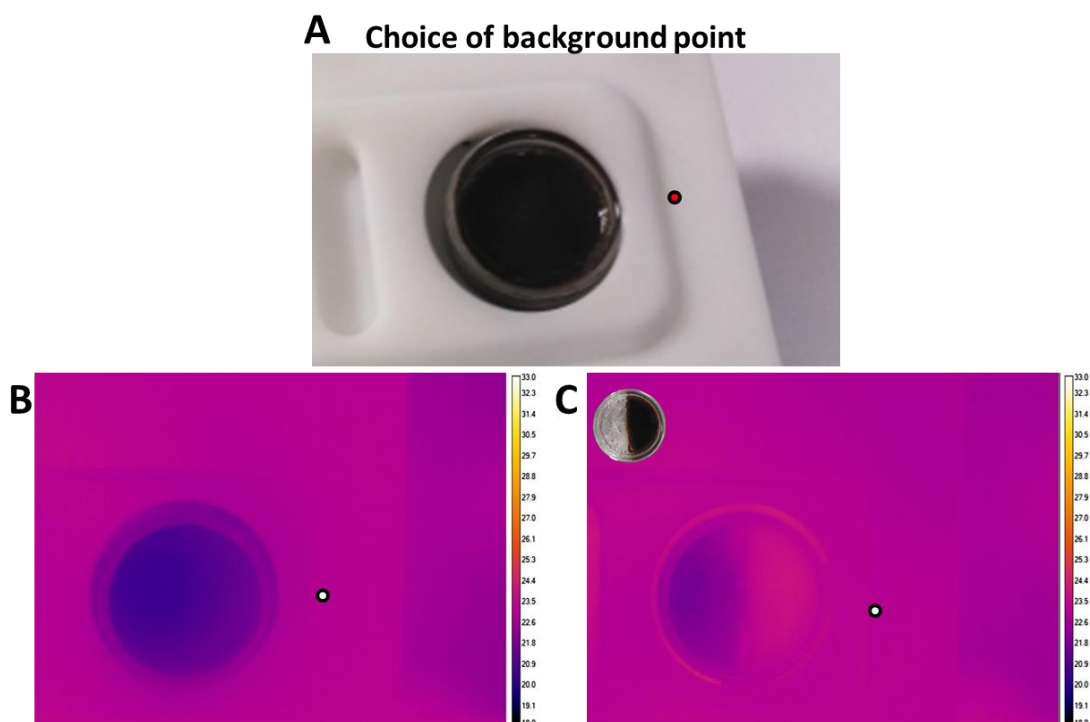


**Figure S4.** Choice of background point (corresponding to Figure 3 in main paper). (A) Optical photograph of the LC-AMF setup with gel placed on Petri dish. Red dot denotes background point used in main paper for analysis in Figure 3. (B) Background choice shown on full thermal image (denoted as white dot). (C) Background choice shown on full thermal image (denoted as white dot).

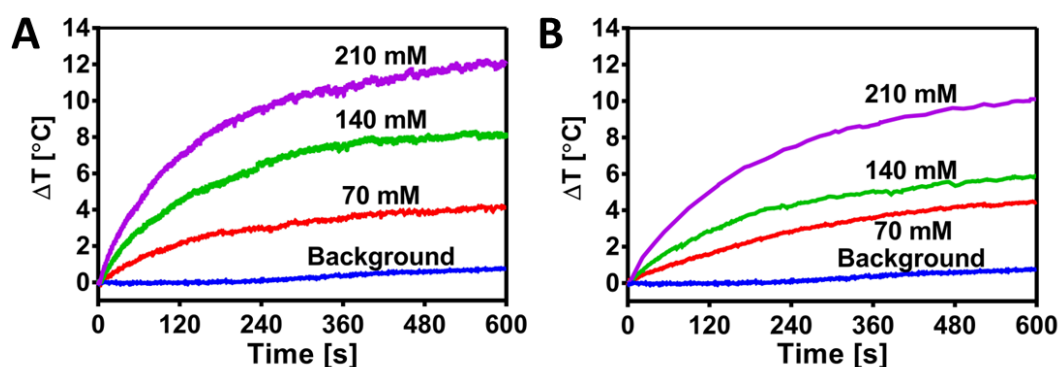


**Figure S5.** (A) Temporal change in temperature ( $\Delta T$ ) plots across the 600 seconds irradiation time for Figure 4A across highest heating points; (B) Average temporal change in temperature ( $\Delta T$ ) plots across the 600 seconds irradiation time for Figure 3A, taken from circular region covering whole sample.

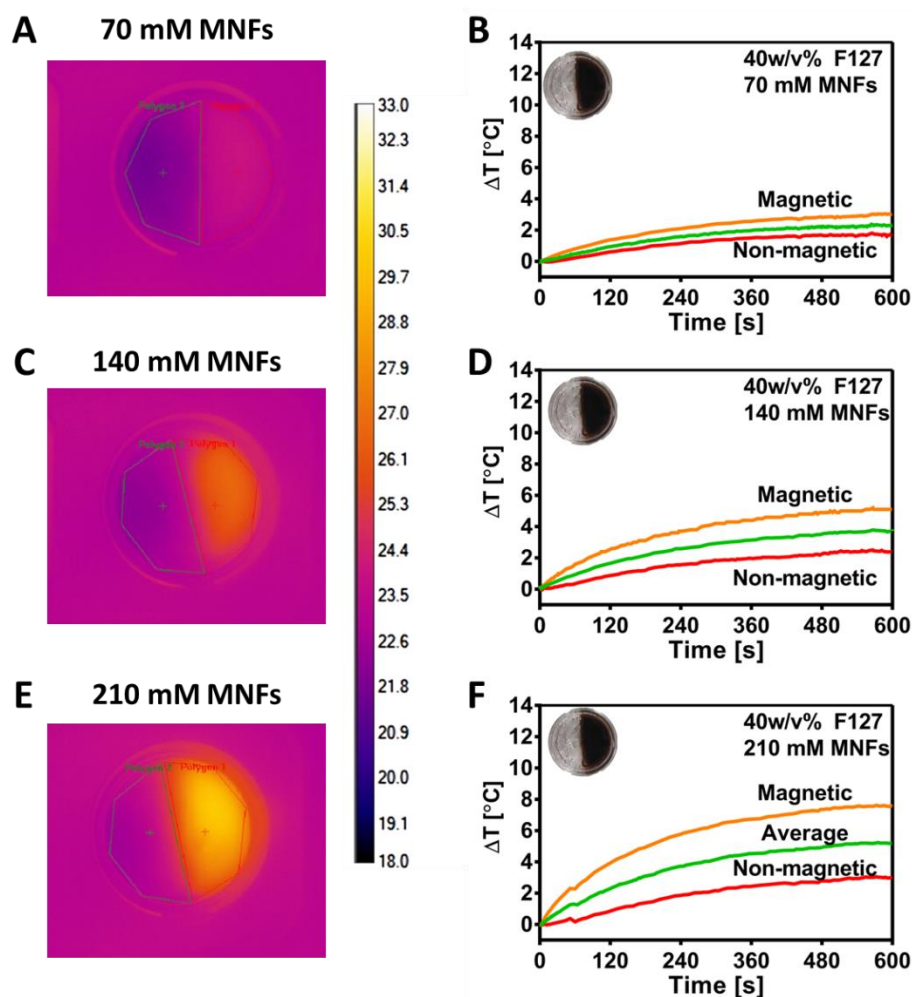


**Figure S6.** In-situ thermography of half-half magnetic and non-magnetic gels with (A) 70mM, (C) 140 mM and (E) 210 mM MNFs loaded 40 w/v% F127. Heating scale bar is common for all images shown here (A, C and E). Software drawn shapes (polygon 2 and polygon 1) are drawn around non-magnetic and magnetic gel halves, respectively. (B), (D) and (F) show associated temporal change in temperature ( $\Delta T$ ) plots across the 600 seconds irradiation time for (A), (C) and (E), respectively with magnetic (polygon 1), non-magnetic (polygon 2) and total whole disc average values taken from circular region covering whole sample.



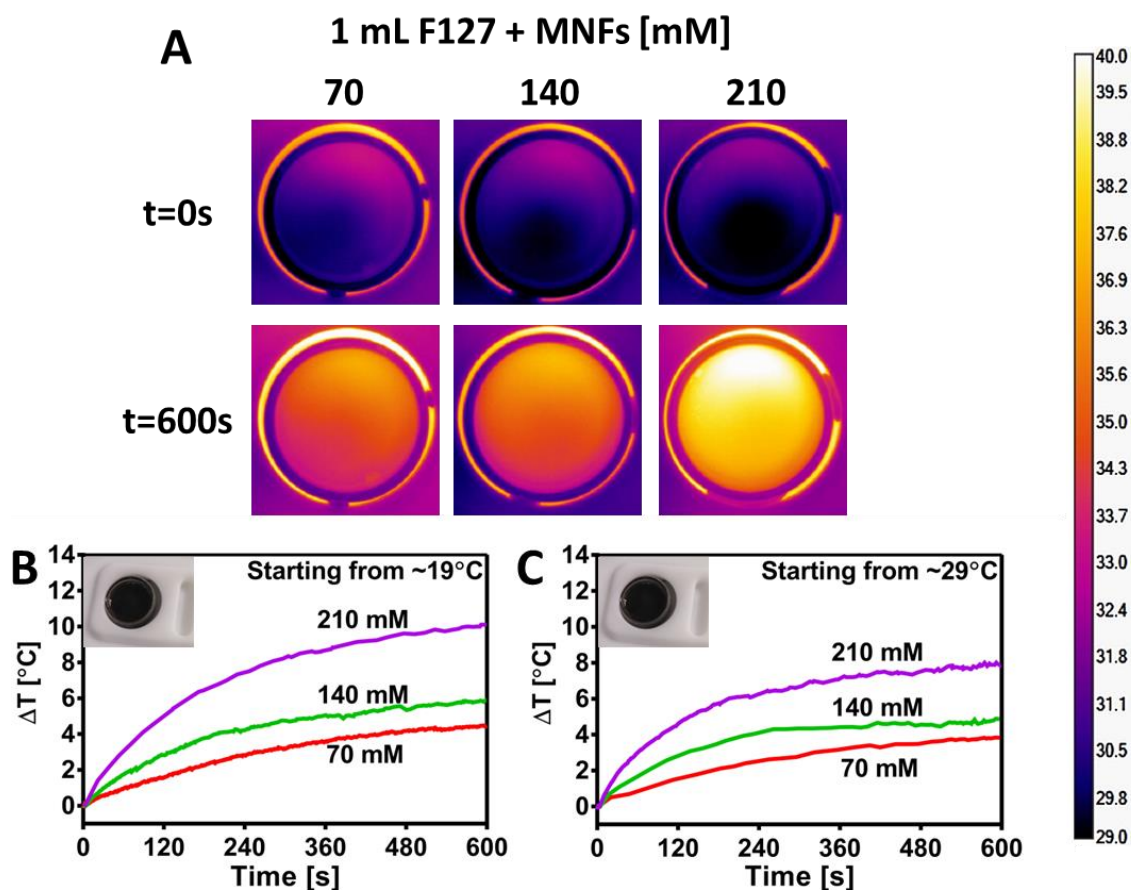


**Figure S7.** (A) In-situ thermography of 1 mL magnetic hydrogels with 70, 140 and 210 mM MNFs 40 w/v% F127. Heating scale bar is common for all images shown in (A). Average temporal change in temperature ( $\Delta T$ ) plots across the 600 seconds irradiation time for (B) Figure 4A from main text and (C) part (A) of this Figure, taken from circular region covering whole sample, with different starting temperatures.

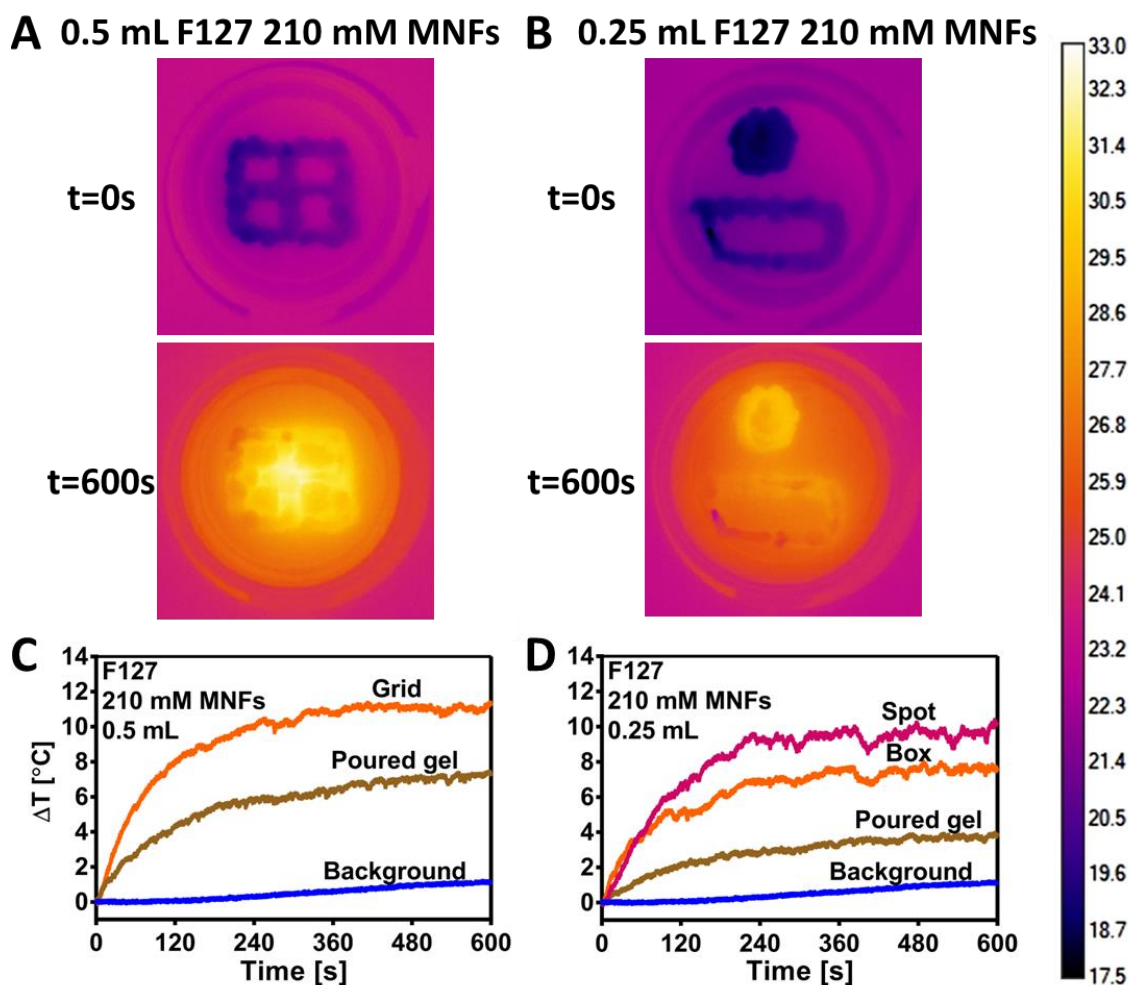


**Figure S8.** Hand-printed structures of 40 w/v% F127 210 mM MNFs of different surface area, but same volume of (A) 0.5 mL and (B) 0.25 mL (compared to previously poured cases in Figure 3E). (C) and (D) associated temporal change in temperature ( $\Delta T$ ) plots across the 600 seconds irradiation time at defined highest heating spots (3x3 pixels) for (A), and (B), respectively. Please note one common thermal scale is provided for A and B. Background is a point defined the same way as shown in Figure S4.

42

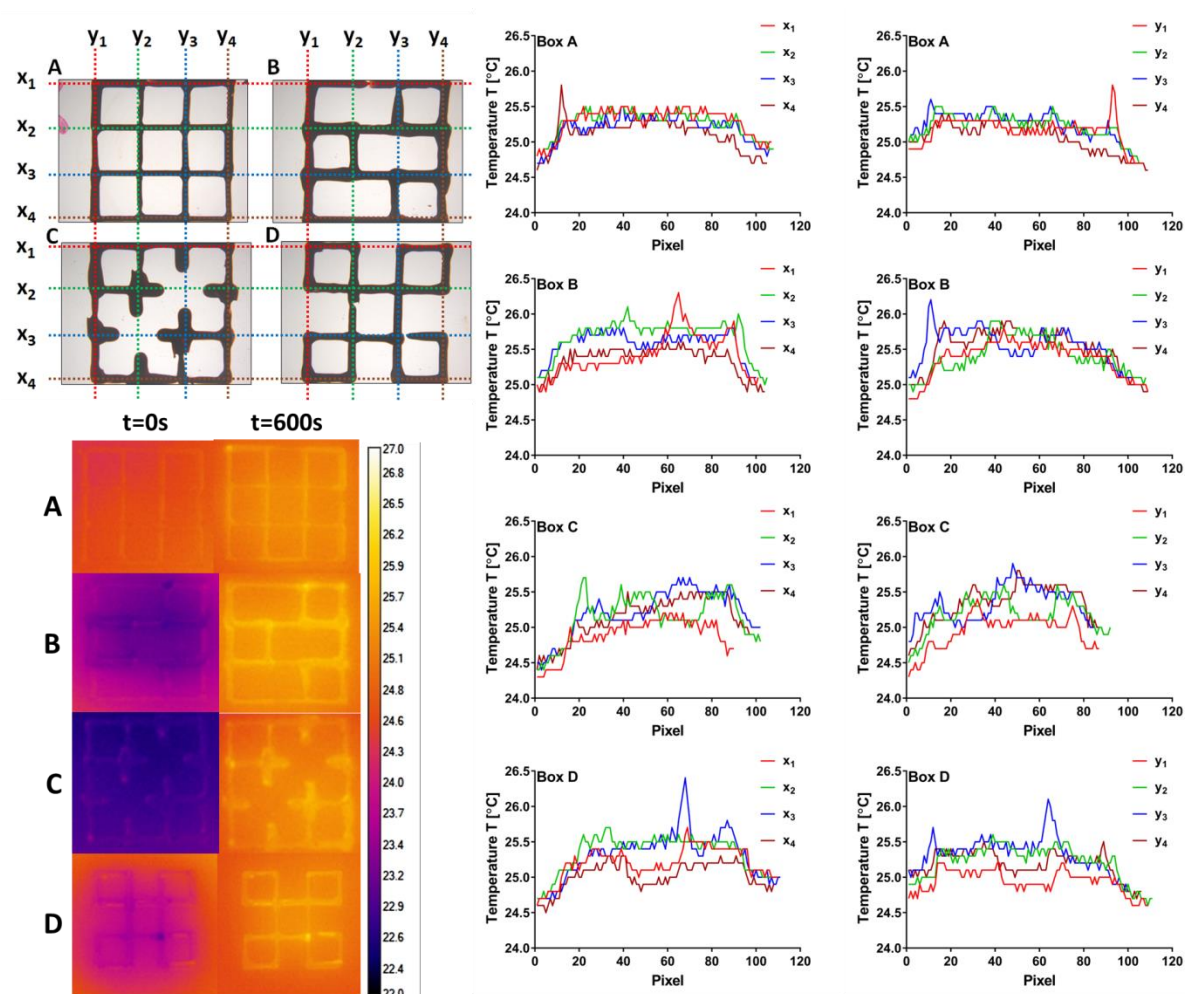


**Figure S10.** “Broken grids” were designed as means to investigate heat dissipation across the grids with purposely interrupted printed paths. Three various designed were used based on original 3 x 3 printed grid (A) with interrupted paths (B-D).

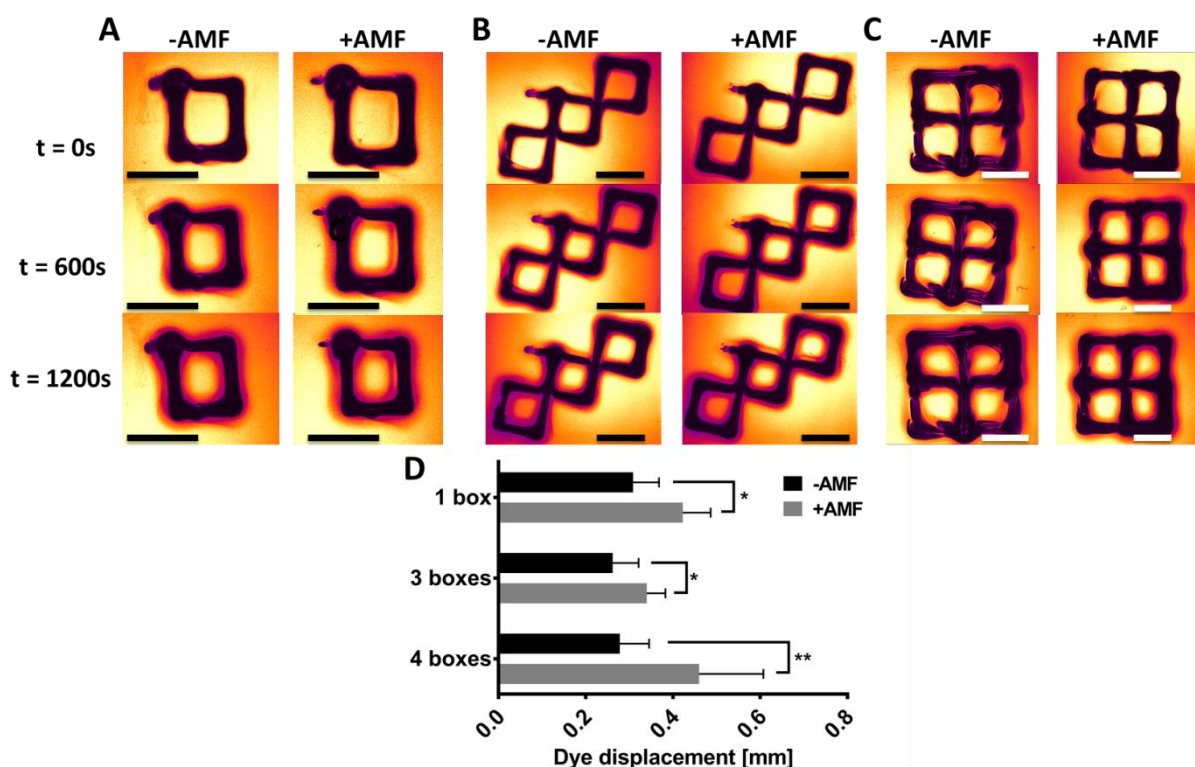


**Figure S11.** Optical measurements of printed (A) single box; (B) diagonal 3 boxes and (C) 4 boxes of MNF-G-714 grids (scale bars = 3 mm) with 0.1 mg mL<sup>-1</sup> methylene blue with and without AMF. (D) Dye displacement represented from the optical images obtained in (A-C). Measurements were taken on middle part of 4 sides (n=4) for (A) and from 8 sides of (B) and (C). Statistical significance was calculated between +AMF and -AMF samples at 1200 s with 95% confidence interval (using unpaired t-test in Graph Pad Prism 7.0). \* denotes P<0.05; \*\* denotes P<0.01.

#### Movies Provided:

**Movie S1:** “Figure 5 5by5 grid.wma”, 90MB, 35 second movie capturing 600s irradiation of the 5\*5 grid shown in Figure 5.

**Movies S2:** “Figure 5 10by10 grid.wma”, 73MB, 35 second movie capturing 600s irradiation of the 10\*10 grid shown in Figure 5.

These grids were printed using MNF-G-2500, and imaged with the A6735sc camera.

**Supporting Gcodes are provided in .gcode format:**

**GS1:** gcode used for printing 5 x 5 grids

**GS2:** gcode used for printing 10 x 10 grids